A multi-tiered map of EMT defines major transition points and identifies vulnerabilities

Indranil Paul[1], Dante Bolzan[3], Heather Hook[4], Ahmed Youssef[1], Gopal Karemore[5], Michael UJ Oliphant[6], Weiwei Lin[1], Qian Liu[7], Sadhna Phanse[1], Carl White[1], Dzmitry Padhorny[10], Sergei Kotelnikov[10], Guillaume Andrieu[8], Pingzhao Hu[7], Gerald V. Denis[9], Dima Kozakov[10], Brian Raught[12], Trevor Siggers[4], Stefan Wuchty[3,11†], Senthil Muthuswamy[6†], Andrew Emili[1,2†*]

Affiliations

[1] Department of Biochemistry, Boston University School of Medicine, Boston University, 72 East Concord Street, Boston, MA 02118, USA

[2] Department of Biology, Charles River Campus, Boston University, Life Science & Engineering (LSEB-602), 24 Cummington Mall, Boston, MA 02215 USA

[3] Department of Computer Science, University of Miami, 1365 Memorial Drive, Coral Gables, FL 33146, USA

[4] (a) Department of Biology, Boston University, 24 Cummington Mall, Boston, MA 02115, USA; (b) Biological Design Center, Boston University, 610 Commonwealth Avenue, Boston, MA 02215

[5] Advanced Analytics, Novo Nordisk A/S, 2760 Måløv, Denmark

[6] Cancer Research Institute, Department of Medicine, Beth Israel Deaconnes Medical Center, Boston MA 02115, USA

[7] Department of Biochemistry and Medical Genetics, University of Manitoba, Winnipeg, Manitoba R3E 0J9, Canada

[8] Team 2 - Institut Necker-Enfants Malades, INSERM U1151, Paris, France

[9] Boston Medical Center Cancer Center, Boston University, Boston University, 72 East Concord Street, Boston, MA 02118, USA

[10] (a) Department of Applied Mathematics and Statistics, Stony Brook University, 11794 Stony Brook, NY. (b) Laufer Center for Physical and Quantitative Biology, Stony Brook University, Stony Brook, New York, 11794, United States

[11] (a) Department of Biology, University of Miami, 1301 Memorial Drive, Coral Gables, FL 33146, USA; (b) Sylvester Comprehensive Cancer Center, 1475 NW 12th Ave, Miami, FL 33136, USA

[12] Discovery Tower (TMDT), 101 College St, Rm. 9-701A, University of Toronto, Toronto, Ontario, M5G 1L7, Canada

† Co-communicating authors

*Correspondence to: aemili@bu.edu

Summary

TGFβ mediated epithelial to mesenchymal transition (EMT) proceeds through hybrid 'E/M' states. A deeper understanding of these states and events which regulate entry to and exit from the E/M states is needed for therapeutic exploitation. We quantified >60,000 molecules across ten time points and twelve omic layers in mammary epithelial cells. Proteomes of whole cells, phosphoproteins, nucleus, extracellular vesicles, secretome and membrane resolved major shifts, E→E/M and E/M→M during EMT, and defined state-specific signatures. Metabolomics identified early activation of arachidonic acid pathway and an enzyme-mediated switch from Cytochrome P450 to Cyclooxygenase / Lipoxygenase branches during E→E/M. Single-cell transcriptomics identified GLIS2 as an early modulator of EMT. Integrative modeling-predicted combinatorial inhibition of AURKB, PP2A and SRC exposed vulnerabilities at E→E/M juncture. Covariance analysis revealed remarkable discordance between proteins and transcripts, and between proteomic layers, implying insufficiency of current approaches. Overall, this dataset provides an unprecedented resource on TGFβ signaling, EMT and cancer.

Short title

Multi-level time-resolved deconstruction of EMT program

Introduction

Epithelial to mesenchymal transition (EMT) regulates cell plasticity during embryonic development, tissue homeostasis and cancer, where polarized epithelial (E) cells dedifferentiate, transition through intermediate E/M hybrid states (E/M) and acquire mesenchymal (M) properties (Nieto et al., 2016). These E/M share several clinically-relevant attributes of circulating tumor cells (CTCs) and are responsible for EMT-associated stemness, chemoresistance, immune evasion and metastasis (Dongre and Weinberg, 2019). Complete molecular characterization of E/M states, and the mechanisms driving E→E/M and E/M→M transitions will enable development of refined mechanistic models and discovery of new therapeutic targets.

Approximately 150 genes are currently described as hallmarks of EMT (MSigDB) (http://www.gsea-msigdb.org/gsea/msigdb/) that were identified from studies measuring the expression of 'endpoint' markers (e.g. CDH1, MUC1, VIM, FN1) to track the process (Sha et al., 2019). The prevalent view on EMT as a transcriptionally-driven program is debatable (Yang et al., 2020). In fact, the poor correlation between genomic alterations or mRNA levels and (sub)cellular proteoforms during EMT has been noted (Califano and Alvarez, 2017; Liu et al., 2016). This is crucial because EMT is likely an emergent property where the shifts in cell physiology and phenotype are orchestrated by intra- and extra-cellular signaling (Sigston and Williams, 2017), extensive receptor-ligand crosstalk, protein relocalization (Hung and Link, 2011) and metabolic adaptations (Tabassum and Polyak, 2015; Thomson et al., 2019). Attempts made to model EMT primarily invoke gene-regulatory networks (GRNs) controlled by key transcription factors (TFs) and miRNAs. These models are usually based on a restricted number of factors and thus do not capture the multi-layered architecture of signaling during EMT (Hong et al., 2015; Zhang et al., 2014). To date, no EMT-focused studies have simultaneously measured metabolite and gene expression changes at different functional levels (e.g., mRNA, total protein, nucleus, secretome, etc.).

Consequentially, several aspects of EMT remain unclear. This includes dependencies between molecular layers, secreted molecules, and specific signatures at various stages of EMT, kinetics and scope of metabolic reprogramming, dynamics of subcellular protein localizations and ligand-receptor mediated intercellular crosstalk. To bridge these gaps, we employed multiple high-throughput platforms including microarray, scRNAseq and precision mass spectrometry (MS) to quantify molecules spanning 12 distinct layers of biological information. Our ability to integrate this information allowed us to define signatures of E/M states and identify molecular regulators of key transition points.

RESULTS

A comprehensive resource on TGFβ-induced EMT

The human mammary epithelial cell line MCF10A has been widely used to investigate TGFβ (transforming growth factor β) induced EMT (Liu et al., 2019b; Wei et al., 2015). To generate extensive temporally resolved quantitative expression maps of the evolving EMT landscape, cells were treated with TGFβ (TGF-β1; 10 ng/mL) over 12 days (0, 4 hrs, 1–6, 8 & 12 days), spanning multiple 'omics' layers and employing complementary technology platforms (**Fig. 1A-B**, **Fig. S1A-C**). Across all time points, after stringent quality control (see **STAR Methods**), we report nanoLC-MS/MS-based quantifications (**Fig. 1C**, **Table S1**) of 6,540 whole cell (*WC*), 4,198 nuclear (*Nuc*), 2,223 plasma membrane (*Mem*), 1,209 extracellular vesicle (*EV*) and 1,133 secreted (*Sec*) proteins. Using a serial enrichment workflow (see **STAR Methods**) we also quantified the total phosphoproteome (*Phos*; 8,741 high-confidence sites on 2,254 proteins; including 6975 Ser, 962 Thr and 140 Tyr residues), N-glycoproteome (*Glyco*; 549 proteins), acetylome (*Acet*; 349 sites on 165 proteins) and peptidome (*Pep*; 547 peptides from 202 proteins). For proteomics, samples for each point were multiplexed using isobaric tandem mass-tag (TMT-10), enabling higher throughput and robust comparisons. In addition to proteins, we tracked cellular metabolism in the same samples by nanoLC-MS/MS-based untargeted metabolomics, quantifying 8,325 HMDB-indexed endogenous small molecules (*Metabol*). Furthermore, we measured 23,787 gene transcripts (mRNA) and 2,578 microRNAs (miRNA) using microarrays. To assess cellular heterogeneity, we employed scRNAseq to quantify transcriptomes of 1,913 individual cells (>200 cells per time point) undergoing EMT.

In total, we provide temporal quantifications of >60,000 proteins, phosphosites, mRNAs, miRNAs, and metabolites combined, in addition to 9,785 mRNAs in our scRNAseq dataset (**Fig. 1C**). Subcellular enrichments were performed using previously established MS-compatible protocols (see **STAR Methods**), yielding high purity determined through keyword matching against a cellular compartment annotation database (**Fig. S1D**). Quantitative reproducibility across the 3 biological replicates was excellent (**Fig. S1E**). The expression profiles in **Fig. 1D** provide a snapshot of concurrent changes of a given gene over various layers during EMT. We reproduced expected expression behavior for many established markers of EMT, including an increase of M markers VIM, CDH2 and concomitant decrease of E markers SCRIB, MUC1. Using strict criteria for differential expression (Benjamini-Hochberg adj. *p-value* < 0.05; $r^2 \geq 0.6$ & $|\log2FC| \geq 1$; see **STAR Methods**) we identified >10,000 significantly regulated molecules (**Table S2**). As such, this study is the largest experimental description of EMT regulome induced by TGFβ, till date.

We found that molecular abundances were highly variable across layers and time-points (**Fig. S1F**) and all layers contributed significantly to the overall variation in the system (**Fig. 1E**). While each layer showed substantive alterations, the magnitudes (**Fig. S1G**), response profiles (**Fig. 1F**) and fraction of differentially expressed molecules (**Fig. 1G**) of each omic data set during the time course varied significantly. These findings provide direct evidence for global reorganization of the cellular architecture during EMT. For example, *Phos* and *Sec* showed the highest fractional change (36% &

128 40%, respectively) (**Fig. 1G**), suggesting extensive intra- and extra-cellular signaling during EMT
129 (Scheel et al., 2011). These results add new depths to our current understanding of TGFβ signaling
130 and EMT (**Fig. 1H, I**).

131

132 Integrative multi-tiered topology of EMT reveals key transition points and identifies 133 molecular drivers

134 Although E→M progression is considered a continuum, distinct stages have been reported for
135 MCF10A cells (Zhang et al., 2014), and cancer tissues (Liu et al., 2019a; Pastushenko et al., 2018).
136 Using a phylogenetic clustering approach (Hughes and Friedman, 2009) we estimated 'distances'
137 between time steps to understand the transition kinetics (**Fig. 2A**). We observed that up to 24 hours
138 cells maintained their parental E phenotype, while day 2 marked a switch-like exit from the E state,
139 suggesting that at day 2 the E/M began and continued through Day 6, after which cells gradually
140 entered the M state. Cells in day 2 to 6 can be further sub-divided into E/M-1 (Day 2/3, late E) and
141 E/M-2 (Day 4/5/6, early M) states. These cellular reconfigurations were consistent with principal
142 component analysis of individual layers, such as *Mem*, *Phos* and *WC* (**Fig. S2A**).

143 Our observations suggest that each molecular layer has a distinct and complementary role in shaping
144 the transition (**Fig 2B**, **Fig 1E-G**, **Fig S1F, G**). Although, the topology was generally correlated (**Fig.
145 2C**), pairwise coefficients of determination (adj. R^2) revealed a strikingly low concordance between
146 total proteins and other proteomic layers (mean R^2 ranging from 0.015 for *Acet* to 0.299 for *Glyco*)
147 (**Fig. 2D, Upper panel**). The discordance was even stronger between mRNA and various proteomic
148 layers (mean R^2 ranging from 0.011 for *Pep* to just 0.109 for *WC*) (**Fig. 2D, Lower panel**), which
149 increased further with EMT progression. Collectively, these observations illustrate that at a systems
150 level mRNA quantity is a poor proxy of protein abundance. Total protein or mRNA quantities are also
151 unreliable predictors of a proteins PTMs or subcellular trafficking, which ultimately determines
152 signaling output.

153 Next, to model the regulatory patterns of molecules, we employed a 3-step computational workflow.
154 First, we used a regression strategy for time-course measurements (Conesa et al., 2006) to remove
155 residual noise (time dimension) and non-reliable (replicates) components. Second, an unsupervised
156 machine learning approach (self-organizing maps, SOMs) (Wirth et al., 2012) was applied on the
157 retained molecules to generate time-point specific SOM portraits (**Fig. 2E, Fig. S2B-D**, see **STAR
158 Methods** for details). SOMs are a powerful integration tool for large and diverse global datasets to
159 extract fundamental underlying patterns of co-regulation (Lu et al., 2009; Tamayo et al., 1999). Third,
160 we performed pathway enrichments (Ulgen et al., 2019) of these SOMs to elucidate the functional
161 themes at each time-step of EMT (**Fig. 2F**).

162 SOMs traced the temporal unfolding of the transition and provided molecular fingerprints of each
163 time-step. Molecules ranking high (top 1% i.e., rank ≤ 250 & log2FC ≥ 1) with SOMs for control to day
164 1 (430 unique molecules) primarily included proteins characteristic of an E state (**Fig. 2E, Table S3**),

such as, ACTG1 (*Mem*; establishes cell junctions and shape) and EPHB2 (*Glyco*; regulates angiogenesis, contact dependent adhesion and migration; tumor suppressor). SOMs for days 6–12 (252 unique molecules) contained established M markers (e.g., CALD1, CDH2, FLNA, FN1, FSTL1, LGALS1, NT5E, TAGLN, TPM1, TPM2, TPM4, VIM). This group included molecules with established roles in cancer and EMT, including miR-5189 (*miR*; targets ARF6 which internalizes CDH1), CALR (*Acet*; Lys 62; calcium homeostasis, promotes metastasis, imparts resistance to anoikis), ALCAM (*Nuc*; prognostic marker in multiple cancers linked to nuclear translocation of β-catenin and stemness), ARHGAP33 (*Sec*; regulates intracellular trafficking), RAPGEF5 (*Sec*; promotes nuclear translocation of β-catenin) and SOCS3 (*Phos*; Thr 3/13; E3 ligase, E3 ligase inhibiting TGFβ signaling). The onset of the major regulatory switch at day 2 is likely driven by molecules peaking at its corresponding SOM (95 molecules) such as miR-675-5p/H19 (*miR*; induces HIF1α, SNAIL activity), LTBP1 (*Sec*; master regulator of integrin-dependent TGFβ activation) and CD44 (*Sec*; signal transduction). Notably, many of the genes/molecules identified in the SOM, to our knowledge, have not been previously linked to TGFβ signaling or EMT, presumably because they do not show clear changes in *mRNA* or *WC* but in 'other' molecular layers, such as *EV* or *Sec* (**Fig. S2E**). This contrasts with most MSigDB hallmarks of EMT for which we captured clear transcriptional profiles (**Fig. S2F**).

Enrichment analysis of active subnetworks (Ulgen et al., 2019) identified 237 significant pathways (**Fig. 2F**, **Table S3**), discretized across sequential steps of EMT. For example, 'Beta oxidation of hexanoyl-CoA to butanoyl-CoA' declined as cells leave E and enter E/M, indicating reprogramming of mitochondrial fatty acid β-oxidation, consistent with a metastatic phenotype (Ma et al., 2018). Conversely, 'RHO GTPases mediated activation of ROCKs/PAKs/IQGAPs' increased as cells leave E/M and enter M, suggestive of their key role at this stage of EMT (Ungefroren et al., 2018). The E/M specifically were associated with migration-associated pathways such as 'anchoring fibril formation', 'ECM proteoglycans' and 'laminin interactions', consistent with their shared property with CTCs.

Overall, we catalogued complex kinetics of thousands of molecules spanning multiple molecular layers during EMT. Importantly, we predict signatures specific to each stage of EMT, e.g., the E/M, with potential clinical value.

Metabolomics reveals kinetics and predicts novel enzyme-metabolite associations

TGFβ is known to regulate Warburg effect in cancer cells, but may also regulate other metabolic pathways with implications for cancer management (Hua et al., 2019). Active subnetwork analysis of *WC* and *Phos* datasets identified 13 enriched KEGG metabolic pathways during TGFβ-induced EMT (**Fig. S3A**). Notably, significant enrichment (*p–value* ≤ 0.05) was only observed post day 2 for pathways such as Steroid biosynthesis (SHB), Sphingolipid metabolism (SLM) and Glycosaminoglycan degradation (GGM). To evaluate these gene-centric inferences of metabolic phenotypes, we directly profiled intra-cellular small molecules by applying an optimized untargeted metabolomics workflow to the same set of samples. Using stringent criteria (see **STAR Methods**), we

202 quantified >8,000 putative HMDB-compounds covering a wide range of chemical classes (**Fig. 3A**).

203 Phylogenetic clustering (**Fig. 3B**) and SOM analysis (**Fig. 3C**) revealed kinetics of metabolic
204 remodeling prompted by TGFβ. In particular, a distinct temporal separation from parental E cells was
205 observed as early as 4 hours indicating rapid modulation of cellular metabolism by TGFβ, preceding
206 changes in most other layers. To glean further insights, we performed integrative network analysis
207 of metabolite SOMs with differential molecules in *WC* and *Phos* using MetaboAnalyst (Chong et al.,
208 2019) (**Fig. 3D**). This analysis reiterated several enriched pathways predicted with protein
209 expression alone, e.g., glycerophospholipid metabolism (GPLM) and lysine degradation (LD).
210 However, integration of metabolite and protein data within the framework of metabolite SOMs
211 revealed pathway activities representative of key transition steps of EMT driven primarily by
212 corresponding metabolite signatures (**Fig. S3B-D**). Indeed, we observed that arachidonic acid
213 metabolism (AAM), GPLM and LD pathways were activated within 4 hours of TGFβ stimulation,
214 which was not captured by gene enrichment. Consistent with observations in **Fig 2F**, processes such
215 as fatty acid metabolism, SHB and SLM appear after day 2, as cells prepare for a metastatic phenotype
216 (Koundouros and Poulogiannis, 2020).

217 Pairwise-correlation based integration of metabolite profiles with proteomics measurements from
218 the same samples could enable mechanistic predictions and aid discovery of novel players. To
219 explore this, we chose AAM as an example. Arachidonic acid is an omega-6 fatty acid stored as
220 membrane phosphoglycerolipid. Its cytosolic release enables stoichiometric chain reactions and
221 results in >100 functionally diverse compounds (Hanna and Hafez, 2018) impacting processes such
222 as redox state, proliferation, apoptosis and chemotaxis (Tallima and El Ridi, 2018). We computed
223 Pearson's correlations between abundance of annotated enzymes, in *WC* and *Phos*, and metabolites
224 of AAM pathway, in *Metabol*, quantified at SOM for 4 hours to day 1 (**Fig. 3E, F**). Overall, we found
225 that metabolites mapping to AAM either increased linearly (CYP450 branch and thromboxane) or
226 initially decreased before rising (Lipoxygenase branch and prostaglandin) (**Fig. 3G**), suggesting fine-
227 tuned regulation of the different branches. Encouragingly, our enzyme-metabolite association map
228 identified PLA2G4A, the rate-limiting phospholipase of AAM pathway (Hanna and Hafez, 2018),
229 among the top candidates (**Fig. 3F**). Interestingly, correlation and expression profiles of PLA2G15,
230 another phospholipase, (**Fig. 3E-G**) indicated a potential enzyme-mediated switch from Cytochrome
231 P450 to Cyclooxygenase/Lipoxygenase branches during E→E/M.

232 Overall, these observations provide direct evidence for the kinetics of metabolic reprogramming
233 during TGFβ induced EMT. We found metabolites and protein signatures coordinating processes
234 such as AAM, GPLM and LD during key stages of the transition. We also demonstrate how our
235 enzyme-metabolite correlation map could be used as a resource to predict novel enzymes for
236 observed metabolic changes.

237

238

scRNAseq analysis reveals heterogeneous responses to TGFβ and novel transcriptional regulators of EMT

scRNAseq studies in murine epithelial Py2T cells treated with TGFβ (Krishnaswamy et al., 2018), MCF10A cells undergoing confluence-dependent EMT (McFaline-Figueroa et al., 2019) and LPS-induced EMT in alveolar epithelial cells (Riemondy et al., 2019), provided critical insights into EMT. However, a temporal analysis of EMT to understand the transition states has not been reported.

After quality control, we retained 1,913 single cells with a combined depth of 9,785 genes (**Fig. S4A, Table S1**). As anticipated, many of the top expressing genes (TGFB1, TPT1, KRT6A, TMSB10, MT2A) are key players in EMT (**Fig. S4B**). Interestingly, similar to many primary human tumors (Aiello et al., 2018; Puram et al., 2018), we did not observe an explicit loss of several classical E markers at the transcript level (**Fig. 4A, Fig. S4C**), indicating post-transcriptional regulation. This may be energetically economical for tumor cells by conferring invasive properties without losing capacity for metastatic seeding (Lambert et al., 2017).

To understand the stages of cell differentiation, we took advantage of the multiple time points in our dataset (as opposed to a 'pseudo-time'), using Monocle3 (see **STAR Methods**) and identified 20 cell clusters in 3 disjoint partitions (**Fig. 4B, Fig. S4D**). Partition P2 (12 clusters) represents the primary EMT axis while P1/P3 predominantly expressed genes related to cell cycle (**Fig. S4E**) and were ignored for further analysis. We observed that C3 responded strongly to TGFβ (**Fig. 4C**), C4/6 resisted EMT, C5/C8 are the 'transition' states and C13/14 represented terminal M cells (in terms of hallmark M markers; **Fig. 4C**, **right panel**). Examining clusters C9/18/19 which were composed of cells from nearly all time points, suggests presence of stable M-type cells in MCF10A populations and appears to be transcriptional impasse to TGFβ signaling.

To explore the underlying gene expression program, we used hierarchical clustering to group the individual clusters into 6 subtypes (**Fig. 4C**) and employed SCENIC (Aibar et al., 2017) to infer TFs and GRNs underlying these subtypes (**Fig. D-F; Table S5**). For each subtype, we identified several unique (**Fig. 4E**) or highly active TFs (**Fig. 4F**), including both established and novel players. Several TFs implicated in EMT (TWIST2, FOXK2, ZEB1, ID2, MSX1, ING4) were over-represented in S4-S6, corresponding to later stages of EMT. In contrast, direct evidence of mechanistic links of TFs enriched in early stages of EMT (i.e., S3, S4) are lacking, indicating gaps in current EMT models. Using human TF–binding arrays (see **STAR Methods, Fig. 4G**) we confirmed elevated activity of three S3 TFs, GLIS2, SP1 and ZNF266 upon TGFβ induction (**Fig. 4H**). In addition to providing experimental evidence to our predictions, the TF-binding array also identified several other TFs potentially playing important roles at the early stages of EMT (**Fig. 4I**).

Overall, we provide a high-resolution temporal map of gene expression programs of individual cells as they respond to TGFβ signaling and undergo EMT. More generally, our data suggests that most transcriptional changes occur at early time points (also **Fig. 2D, Lower panel**), followed by further adaptations driven predominantly by secondary or post-transcriptional mechanisms.

Spatial regulation of proteins and inter-cellular communication during EMT

Regulation of protein distribution is a crucial signaling mechanism (Ferrell, 1998), but remains insufficiently understood in EMT. The average pairwise Pearson's correlation between proteins quantified in various cellular compartments (CCs) ranged between r = 0.12 to 0.58 indicating fine-tuned regulation of protein distributions (**Fig. 5A**). We found 3,965 proteins localizing to ≥2 CCs (**Fig. S5A**), which we categorized into 2 classes as follows: Class I proteins (1,424) displayed a correlated trend ($r \geq 0.4$) consistently across all CC pairs suggesting regulation primarily at or before the translation step (**Fig. 5B, C; Table S5**). Class II proteins (1,205) displayed anti-correlated trends ($r \leq -0.4$) between any two CCs, active post-translational control of their asymmetric distributions (**Fig. 5D, E; Table S5**).

The Bromodomain and ExtraTerminal (BET) cofactors, BRD2 and BRD4, were identified as Class II proteins, with contrasting kinetic profiles (**Fig. 5F**). Using TF-binding arrays, we verified enhanced global recruitment of BRD4, but not two other cofactors p300 and LSD1, (**Fig. 5G**) indicating its importance during EMT. Indeed, treatment with a pan-BET inhibitor JQ-1 suppressed EMT (**Fig. 5H**). Another notable Class II protein was SCRIB (**Fig. 5I**), which regulates apical-basal polarity and directional migration by acting as a molecular scaffold through protein-protein interactions (Bonello and Peifer, 2019). Using an *in* vivo proximity ligation (BioID) screen of SCRIB ((**Fig. S5B**, see **STAR Methods**), we identified multiple novel interactors (**Table S6**) of which many have known roles in EMT (**Fig. 5J**). Using immunoprecipitation, we verified interactions of SCRIB with SNAP23 and ARHGEF7 (**Fig. 5K**).

Regulation of extracellular signals is important for EMT (Scheel et al., 2011). Subtypes within a cell population can differ in their capacity to send and receive signals, with implications for metastasis and drug resistance (Kim et al., 2018; Tabassum and Polyak, 2015). To map the inter-cellular communication between subgroups of cells during TGFβ-induced EMT, we integrate proteomics and scRNAseq data to perform a systems-wide survey of ligand-receptor (L-R) pair mediated crosstalk (**Fig. 5L**).

First, using a database of >2,500 curated binary L-R interactions (Ramilowski et al., 2015), we searched for pairs of L and R in our *Sec* and *Mem/Glyco* datasets, respectively, assuming that co-directional expression changes in L and/or R of a pair (FDR adj. *p-value* < 0.05 and combined L-R |log2FC| ≥1) can indicate biological role. Currently, at least two L-R pairs are implicated in TGFβ-induced EMT in several tissue models (Heldin et al., 2012). Our analysis detected 67 upregulated and 12 downregulated L-R pairs at any given time point (**Fig. 5M, Table S7**) following TGFβ treatment. Notably, none of these pairs have been directly implicated in TGFβ signaling or EMT, although individually many of the identified L or R occur frequently in the context of EMT and/or cancer. For instance, LAMC2 with its 7 receptors (CD151, COL17A1, ITGA2, ITGA3, ITGA6, ITGB1, ITGB4) exhibit significant alteration during EMT. LAMC2 is overexpressed in cancers (Garg et al., 2014) and its silencing can reverse EMT (Moon et al., 2015; Pei et al., 2019). The cognate receptors, CD151, ITGA3, ITGA6 and ITGB1 synergize with TGFβ signaling to promote metastatic behavior (Pellinen et al.,

314 2018; Sadej et al., 2010; Shirakihara et al., 2013; Zhang et al., 2017).

315 Next, by systematically comparing the expression patterns of L & R (identified above) among the 16
316 clusters (identified in our scRNAseq dataset), we obtained cell-cell communication networks (sender
317 → receiver) (**Fig. 5N, Fig. S5C, Table S7**). For example, C13 cells, which appeared at day 3 and
318 showed highest M genes expression (**Fig. 4C**), produced the receptor CD44 to its cognate ligand
319 MMP7 expressed by C17 (**Fig. S5D**). Together, this suggests that communication between cell
320 subgroups (C17:MMP7 → C13:CD44) may exist during EMT which can have potential ramifications
321 for tumor growth (Tabassum and Polyak, 2015). Encouragingly, several of these identified L-R pairs
322 showed strong correlation (**Fig. 5O**) in human breast invasive carcinoma samples (Cancer Genome
323 Atlas Network, 2012; Cerami et al., 2012).

324 Our study provides a comprehensive analysis of TGFβ-triggered subcellular trafficking as cells
325 undergo EMT. Such translocations, potentially driven by differential PPI, could mediate the tight
326 coordination between functional modules (e.g., SCRIB complex) and EMT phenotypes such as
327 cytoskeletal rearrangement (Huang et al., 2012). We also uncovered novel cell-cell communication
328 pathways via L-R interactions in driving EMT, representing an untapped clinical opportunity.

329

330 Modeling phosphoproteome dynamics during EMT reveals kinase susceptibilities

331 Phosphoregulatory mechanisms are a key aspect of TGFβ signaling and EMT. We confidently
332 quantified 8,741 phosphosites (p-sites; 6,975 Ser, 962 Thr and 140 Tyr residues) (**Fig. S6A-C**) over a
333 dynamic range of 10^6 orders of magnitude (**Fig. S6D**), and phospho–STY frequencies (**Fig. S6E**) in
334 line with previous reports (D'Souza et al., 2014) mapping to 2,254 proteins (**Fig. S6F**). Of all p-sites,
335 3,138 (35.8%) were differentially regulated in at least one time point (**Fig. S6G**). At protein level,
336 different patterns of regulation were noted; some proteins, such as DEK, VIM and MISP, were
337 regulated at ~90% of detected sites, some proteins, such as CAV1, CAMK2 and GOLGA1, showed a
338 ~50% mixture of regulated and unregulated sites, while others such as AHNAK, PML and BCLAF1
339 showed ~2% differential sites (**Fig. 6A**). Interestingly, the fraction of regulated p-sites in several
340 proteins, e.g., VIM, increased with EMT progression (**Fig. 6B**).

341 We observed that in ~50%, p-sites dynamics were not explained ($r \leq 0.4$) by a corresponding change
342 at the protein level (**Fig. 6C, D**). Interestingly, for ~26%, a directionally opposite change between
343 phosphorylation and the corresponding protein abundance was noted ($r \leq -0.1$), suggesting effects
344 on protein stability. Phospho-regulated proteins were enriched for '*nucleus*', '*cytoskeleton*' and '*focal*
345 *adhesion*' annotations (**Fig. 6E**) reflecting the importance of CC remodeling during EMT.

346 We also computed correlations between nuclear localization profiles (*Nuc*) and phosphorylation
347 kinetics (*Phos*) of individual proteins (**Fig. 6F, G**). For instance, phosphorylation of MICAL3 at T684
348 and S685 regulates CSCs by promoting symmetric division (Tominaga et al., 2019). The pattern of
349 phosphorylation at residues T684, S685 and S687 (**Fig. 6D,** MICAL3) which are located at the

350 consensus NLS motif of MICAL3 suggests a role in regulating nuclear translocation and/or retention
351 at E/M→M transition. Indeed, the bipartite NLS motif of MICAL3 interacts with Importin-α and the
352 p-sites T684, S685, S687 are directly adjacent to the binding interface (**Fig. 6H**).

353 To analyze stage-specific kinase activities we generated a ternary model which distinguishes active
354 kinases into 3 broad stages (i.e., E, E/M, and M) of EMT (**Fig. 6I, Fig. S6H**). An example that illustrates
355 the utility of this model are AKT isoforms that have distinct and opposing roles during cancer
356 development (Hinz and Jücker, 2019). We predict AKT1 is strongly associated with the E-stage, which
357 is consistent with its role in maintaining the E phenotype (Li et al., 2016). In fact, depletion of AKT1
358 in MCF10A cells promoted TGFβ-induced E→E/M transition (Iliopoulos et al., 2009). Our model
359 further predicts key roles for AKT2 and AKT3 at E/M→M transition. Indeed, AKT2 and AKT3 were
360 associated with tumor invasiveness, stemness and sensitivity to drug treatment (Chin et al., 2014),
361 key characteristics of the E/M populations (Dongre and Weinberg, 2019). Among several other
362 kinases (**Fig. S6J**), our ternary model predicts critical roles for PRKCA and AURKB at the junction of
363 E→E/M and E/M→M transitions. PRKCA is reportedly a hub and therapeutic target for EMT-induced
364 breast CSCs (Tam et al., 2013). Similarly, inhibition of AURKB was found to reverse EMT and reduce
365 breast cancer metastasis *in vivo* (Zhang et al., 2020).

366 Overall, we reveal the rich intricacies of the phosphoregulome during EMT, identified functional p-
367 sites, predict novel kinase susceptibilities, and provide a mechanistic framework to enhance
368 understanding of the signaling mechanisms during EMT.

369

370 Integrative systems causal model of EMT identifies mechanistic vulnerabilities

371 Systems biology approaches that combine multiple molecular types (proteins, miRNAs, metabolites)
372 into a framework of established knowledge allow for a rich assessment of a biological context (Hawe
373 et al., 2019; Karczewski and Snyder, 2018). Using experimentally validated functional priors
374 (compiled from ENCODE, PhosphoSitePlus, SignaLink 2.0, SIGNOR 2.0, HINT, miRTarBase and
375 MetaBridge), we combined causal inference and PCSF (Prize Collecting Steiner Forest) (Akhmedov
376 et al., 2017) to construct hierarchical mechanistic models of the EMT program (**Fig. 7A**, see **STAR**
377 **Methods**). The final 'EMT network' comprised of 3,255 edges connecting 2,217 molecules, including
378 723 kinase/phosphatase–substrate, 1,407 TF–target, 746 miRNA–target and 31 metabolite–gene
379 interactions.

380 One of the potential applications of the EMT network is to discover signaling paths from TGFBR1/2
381 to any gene(s) of interest within the network. As a demonstration, we queried several genes (FN1,
382 MMP7, CD44, SCRIB, TWISTNB, ZEB1, SNAI2) and recovered previously known and unknown paths
383 to them putatively active at multiple stages of EMT (**Fig. 7B**). Next, to identify key factors driving
384 EMT, we extracted 'controller' nodes exerting a significant influence on EMT network topology (see
385 **STAR Methods**). Survival analysis against a large publicly available dataset of primary breast cancers
386 with long-term patient outcomes (Cancer Genome Atlas Network, 2012) showed a significant

387 association between tumors with altered expression of these controllers and shortened overall
388 survival (**Fig. 7C**). Not surprisingly, a few of them are established key regulators of metastasis (**Fig.**
389 **7D**), providing independent support to our model. Unlike controllers, however, the non-controller
390 nodes were poorly represented in EMT literature (**Fig. 7E**), again highlighting gaps, and potentially
391 identifying new regulatory processes.

392 We queried the EMT network to identify the signaling context in which these controllers are active
393 at various key stages of EMT, which could also provide clues into mechanistic vulnerabilities (**Fig.**
394 **7F**). As cells are stimulated with TGFβ, the TFs SMAD2 and SMAD3 are activated, as expected. Another
395 early responder was RHO GTPase RAC1, an effector of both KRAS (Wu et al., 2014) and TGFβ signaling
396 (Ungefroren et al., 2018), suggesting potential crosstalk. The downstream effector of RAC1, MAPK14
397 (p38 MAPK), was also regulated early in EMT, suggesting cooperation between RAC1 and MAPK
398 pathways (Santibáñez et al., 2010). Our model suggests SMAD3 regulates two other TF hubs, CEBPB
399 (CCAAT/enhancer-binding protein β) and FOXA1. Loss of CEBPB reportedly switches TGFβ signaling
400 from growth-inhibiting to EMT-inducing (Johansson et al., 2013), while FOXA1 is reportedly a key TF
401 during EMT (Wang et al., 2013). We observed that STAT3 is suppressed at later stages of EMT. A
402 recent study in KRAS-driven lung and pancreatic cancer found that STAT3 is required for maintaining
403 the E state and is lost during acquisition of M phenotypes (D'Amico et al., 2018).

404 The EMT network directly predicts novel avenues for blocking EMT. To assess this, we performed a
405 morphometry-based screening where we treated MCF10A cells with TGFβ in combination with drugs
406 which were predicted to inhibit several of the controller nodes active at E→E/M transition (**Fig. 7G,**
407 see **STAR Methods**). Our analysis using a custom-built and publicly accessible image analysis
408 software (Ochs et al., 2019) (**Fig. 7G**) showed noticeable efficacy of LB100+Barasertib, LB100+PP1
409 and Sonidegib+Autocamtide in reverting the elongated (= 'eccentric') phenotype of EMT-induced
410 cells (**Fig. 7H**), thus providing direct experimental evidence to our predictions.

411 Overall, our EMT network recapitulates known signaling pathways, uncovers novel routes of
412 information flow to known regulators of EMT, identifies new signaling players and pathways, makes
413 substantial and provocative novel predictions and reveals cohesive time-resolved regulatory
414 patterns and mechanistic links between both controllers and non-controllers.

415

416 DISCUSSION

417 EMT and cancer are *emergent systems* (Sigston and Williams, 2017) wherein progression through
418 various stages is regulated by intricate networks of intra- and extra-cellular signaling within and
419 between cells. The key to understanding such complex biological phenomena are establishing
420 experimental workflows that integrate multiple tiers of biological information (Karczewski and
421 Snyder, 2018).

422 Theoretical discussions on EMT are often guided by the Waddington metaphor of a ball (=cell) rolling
423 over a phenotypic landscape, which is dynamically shaped by multiple parameters: topologies of

signaling networks, molecular stochasticity, extraneous cooperating and opposing forces (e.g., EMT inducing and/or inhibitory ligands, interaction with other cells) (Li and Balazsi, 2018). By integrating several molecular layers, SOMs and 'neighbor joining' approaches revealed the kinetics of cell-fate transitions and major phenotypic switch points driven by TGFβ. Several studies have indicated molecular and phenotypic granularity in EMT continuum and suggested existence of discrete metastable E/M (Sha et al., 2019). Many current EMT markers are biased toward the later stages of EMT, when the process is approaching completion (Song et al., 2019). Consequently, the molecular nature of E/M is still poorly understood. Our time-course integrative SOM allowed us to trace the temporal unfolding and uncover the molecular nature of the E→M transition.

While previous omics studies have measured either one or two molecular layers to describe EMT, our multi-tiered datasets enabled the discovery of several new aspects of EMT which were not captured by previous approaches. For example, the correlation between *mRNA* and proteins were weak. Strikingly, correlations between the various *proteomics layers* were also found to be quite poor, indicating that systems behavior cannot readily be extrapolated by any single layer (e.g., mRNA or total proteome), but instead needs an integrated analysis of several molecular layers. We show that TGFβ-induced EMT is only partially driven by transcription, where several E genes are repressed only post-transcriptionally, while transcripts of M genes are upregulated but mostly during earlier time points. At later stages, post-translational mechanisms become more prominent in driving the process, suggesting that the regulatory control of EMT may be more flexible than previously appreciated. Similarly, our results also predict the mechanistic importance of protein subcellular localization during EMT. A comparison of proteins detected in *EV*, *Sec*, *Glyco*, *Mem* and *Nuc* indicated extensive regulation of protein localizations. Further, previous studies on EMT have largely focused on cell-autonomous signaling, whereas multiple inter-cellular signaling mechanisms are evident from our integrative analysis. Indeed, we found both *EV* and *Sec* to be extensively regulated during EMT. Once considered as cellular 'garbage bins', their active participation in signaling and crosstalk is increasingly recognized (H. Rashed et al., 2017). Our results demonstrating limited qualitative overlap between *EV* and *Sec* hint at a potentially overlooked mechanistic distinction and provides opportunities for new biological insights. We utilized our *Mem*, *Glyco* and *Sec* datasets to provide a repertoire of 79 putative new L-R pairs with potential roles during EMT, which should be validated in future studies. By combining these results with the scRNAseq profiles, we were able to define an extensive network of inter-cellular communications.

In conclusion, we have established a comprehensive multi-tiered molecular landscape of TGFβ-induced EMT. This study aims to provide a valuable resource which is accessible through an interactive website (https://srphanse.shinyapps.io/EMTAPP_2/) (**Fig. S7**) and will strongly complement hypothesis-driven research with direct implications for epithelial cancers.

461 # REFERENCES

462 Aibar, S., González-Blas, C.B., Moerman, T., Huynh-Thu, V.A., Imrichova, H., Hulselmans, G., Rambow,
463 F., Marine, J.-C., Geurts, P., Aerts, J., et al. (2017). SCENIC: Single-cell regulatory network inference
464 and clustering. Nat. Methods *14*, 1083–1086.

465 Aiello, N.M., Maddipati, R., Norgard, R.J., Balli, D., Li, J., Yuan, S., Yamazoe, T., Black, T., Sahmoud, A.,
466 Furth, E.E., et al. (2018). EMT Subtype Influences Epithelial Plasticity and Mode of Cell Migration.
467 Dev. Cell *45*, 681-695.e4.

468 Akhmedov, M., Kedaigle, A., Chong, R.E., Montemanni, R., Bertoni, F., Fraenkel, E., and Kwee, I.
469 (2017). PCSF: An R-package for network-based interpretation of high-throughput data. PLOS
470 Comput. Biol. *13*, e1005694.

471 Bonello, T.T., and Peifer, M. (2019). Scribble: A master scaffold in polarity, adhesion,
472 synaptogenesis, and proliferation. J. Cell Biol. *218*, 742–756.

473 Califano, A., and Alvarez, M.J. (2017). The recurrent architecture of tumour initiation, progression
474 and drug sensitivity. Nat. Rev. Cancer *17*, 116–130.

475 Cancer Genome Atlas Network (2012). Comprehensive molecular portraits of human breast
476 tumours. Nature *490*, 61–70.

477 Cerami, E., Gao, J., Dogrusoz, U., Gross, B.E., Sumer, S.O., Aksoy, B.A., Jacobsen, A., Byrne, C.J., Heuer,
478 M.L., Larsson, E., et al. (2012). The cBio Cancer Genomics Portal: An Open Platform for Exploring
479 Multidimensional Cancer Genomics Data: Figure 1. Cancer Discov. *2*, 401–404.

480 Chin, Y.R., Yoshida, T., Marusyk, A., Beck, A.H., Polyak, K., and Toker, A. (2014). Targeting Akt3
481 Signaling in Triple-Negative Breast Cancer. Cancer Res. *74*, 964–973.

482 Chong, J., Wishart, D.S., and Xia, J. (2019). Using MetaboAnalyst 4.0 for Comprehensive and
483 Integrative Metabolomics Data Analysis. Curr. Protoc. Bioinforma. *68*, e86.

484 Conesa, A., Nueda, M.J., Ferrer, A., and Talón, M. (2006). maSigPro: a method to identify significantly
485 differential expression profiles in time-course microarray experiments. Bioinforma. Oxf. Engl. *22*,
486 1096–1102.

487 D'Amico, S., Shi, J., Martin, B.L., Crawford, H.C., Petrenko, O., and Reich, N.C. (2018). STAT3 is a
488 master regulator of epithelial identity and KRAS-driven tumorigenesis. Genes Dev. *32*, 1175–1187.

489 Dongre, A., and Weinberg, R.A. (2019). New insights into the mechanisms of epithelial–
490 mesenchymal transition and implications for cancer. Nat. Rev. Mol. Cell Biol. *20*, 69–84.

491 D'Souza, R.C.J., Knittle, A.M., Nagaraj, N., Dinther, M. van, Choudhary, C., Dijke, P. ten, Mann, M., and
492 Sharma, K. (2014). Time-resolved dissection of early phosphoproteome and ensuing proteome
493 changes in response to TGF-β. Sci. Signal. *7*, rs5–rs5.

494 Ferrell, J.E. (1998). How regulated protein translocation can produce switch-like responses. Trends
495 Biochem. Sci. *23*, 461–465.

496 Garg, M., Braunstein, G., and Koeffler, H.P. (2014). LAMC2 as a therapeutic target for cancers. Expert
497 Opin. Ther. Targets *18*, 979–982.

498 H. Rashed, M., Bayraktar, E., K. Helal, G., Abd-Ellah, M.F., Amero, P., Chavez-Reyes, A., and Rodriguez-
499 Aguayo, C. (2017). Exosomes: From Garbage Bins to Promising Therapeutic Targets. Int. J. Mol. Sci.
500 *18*.

501 Hanna, V.S., and Hafez, E.A.A. (2018). Synopsis of arachidonic acid metabolism: A review. J. Adv. Res.
502 *11*, 23–32.

503 Hawe, J.S., Theis, F.J., and Heinig, M. (2019). Inferring Interaction Networks From Multi-Omics Data.
504 Front. Genet. *10*.

505 Heldin, C.-H., Vanlandewijck, M., and Moustakas, A. (2012). Regulation of EMT by TGFβ in cancer.
506 FEBS Lett. *586*, 1959–1970.

507 Hinz, N., and Jücker, M. (2019). Distinct functions of AKT isoforms in breast cancer: a
508 comprehensive review. Cell Commun. Signal. CCS *17*.

509 Hong, T., Watanabe, K., Ta, C.H., Villarreal-Ponce, A., Nie, Q., and Dai, X. (2015). An Ovol2-Zeb1
510 Mutual Inhibitory Circuit Governs Bidirectional and Multi-step Transition between Epithelial and
511 Mesenchymal States. PLOS Comput. Biol. *11*, e1004569.

512 Hua, W., ten Dijke, P., Kostidis, S., Giera, M., and Hornsveld, M. (2019). TGFβ-induced metabolic
513 reprogramming during epithelial-to-mesenchymal transition in cancer. Cell. Mol. Life Sci.

514 Huang, R.Y.-J., Guilford, P., and Thiery, J.P. (2012). Early events in cell adhesion and polarity during
515 epithelial-mesenchymal transition. J. Cell Sci. *125*, 4417–4422.

516 Hughes, A.L., and Friedman, R. (2009). A phylogenetic approach to gene expression data: evidence
517 for the evolutionary origin of mammalian leukocyte phenotypes. Evol. Dev. *11*, 382–390.

518 Hung, M.-C., and Link, W. (2011). Protein localization in disease and therapy. J. Cell Sci. *124*, 3381–
519 3392.

520 Iliopoulos, D., Polytarchou, C., Hatziapostolou, M., Kottakis, F., Maroulakou, I.G., Struhl, K., and
521 Tsichlis, P.N. (2009). MicroRNAs differentially regulated by Akt isoforms control EMT and stem cell
522 renewal in cancer cells. Sci. Signal. *2*, ra62.

523 Johansson, J., Berg, T., Kurzejamska, E., Pang, M.-F., Tabor, V., Jansson, M., Roswall, P., Pietras, K.,
524 Sund, M., Religa, P., et al. (2013). MiR-155-mediated loss of C/EBPβ shifts the TGF-β response from
525 growth inhibition to epithelial-mesenchymal transition, invasion and metastasis in breast cancer.
526 Oncogene *32*, 5614–5624.

527 Karczewski, K.J., and Snyder, M.P. (2018). Integrative omics for health and disease. Nat. Rev. Genet.
528 *19*, 299–310.

529 Kim, E., Kim, J.-Y., Smith, M.A., Haura, E.B., and Anderson, A.R.A. (2018). Cell signaling heterogeneity
530 is modulated by both cell-intrinsic and -extrinsic mechanisms: An integrated approach to
531 understanding targeted therapy. PLoS Biol. *16*.

532 Koundouros, N., and Poulogiannis, G. (2020). Reprogramming of fatty acid metabolism in cancer. Br.
533 J. Cancer *122*, 4–22.

534 Krishnaswamy, S., Zivanovic, N., Sharma, R., Pe'er, D., and Bodenmiller, B. (2018). Learning time-
535 varying information flow from single-cell epithelial to mesenchymal transition data. PLoS ONE *13*.

536 Lambert, A.W., Pattabiraman, D.R., and Weinberg, R.A. (2017). Emerging Biological Principles of
537 Metastasis. Cell *168*, 670–691.

538 Li, C., and Balazsi, G. (2018). A landscape view on the interplay between EMT and cancer metastasis.
539 Npj Syst. Biol. Appl. *4*, 1–9.

540 Li, C.-W., Xia, W., Lim, S.-O., Hsu, J.L., Huo, L., Wu, Y., Li, L.-Y., Lai, C.-C., Chang, S.-S., Hsu, Y.-H., et al.
541 (2016). AKT1 Inhibits Epithelial-to-Mesenchymal Transition in Breast Cancer through
542 Phosphorylation-Dependent Twist1 Degradation. Cancer Res. *76*, 1451–1462.

543 Liu, X., Li, J., Cadilha, B.L., Markota, A., Voigt, C., Huang, Z., Lin, P.P., Wang, D.D., Dai, J., Kranz, G., et al.
544 (2019a). Epithelial-type systemic breast carcinoma cells with a restricted mesenchymal transition
545 are a major source of metastasis. Sci. Adv. *5*, eaav4275.

546 Liu, Y., Beyer, A., and Aebersold, R. (2016). On the Dependency of Cellular Protein Levels on mRNA
547 Abundance. Cell *165*, 535–550.

548 Liu, Y., Xue, M., Du, S., Feng, W., Zhang, K., Zhang, L., Liu, H., Jia, G., Wu, L., Hu, X., et al. (2019b).
549 Competitive endogenous RNA is an intrinsic component of EMT regulatory circuits and modulates
550 EMT. Nat. Commun. *10*, 1637.

551 Lu, R., Markowetz, F., Unwin, R.D., Leek, J.T., Airoldi, E.M., MacArthur, B.D., Lachmann, A., Rozov, R.,
552 Ma'ayan, A., Boyer, L.A., et al. (2009). Systems-level dynamic analyses of fate change in murine
553 embryonic stem cells. Nature *462*, 358–362.

554 Ma, Y., Temkin, S.M., Hawkridge, A.M., Guo, C., Wang, W., Wang, X.-Y., and Fang, X. (2018). Fatty acid
555 oxidation: An emerging facet of metabolic transformation in cancer. Cancer Lett. *435*, 92–100.

556 McFaline-Figueroa, J.L., Hill, A.J., Qiu, X., Jackson, D., Shendure, J., and Trapnell, C. (2019). A pooled
557 single-cell genetic screen identifies regulatory checkpoints in the continuum of the epithelial-to-
558 mesenchymal transition. Nat. Genet. *51*, 1389–1398.

559 Moon, Y.W., Rao, G., Kim, J.J., Shim, H.-S., Park, K.-S., An, S.S., Kim, B., Steeg, P.S., Sarfaraz, S.,
560 Changwoo Lee, L., et al. (2015). LAMC2 enhances the metastatic potential of lung adenocarcinoma.
561 Cell Death Differ. *22*, 1341–1352.

562 Nieto, M.A., Huang, R.Y.-J., Jackson, R.A., and Thiery, J.P. (2016). EMT: 2016. Cell *166*, 21–45.

563 Ochs, F., Karemore, G., Miron, E., Brown, J., Sedlackova, H., Rask, M.-B., Lampe, M., Buckle, V.,
564 Schermelleh, L., Lukas, J., et al. (2019). Stabilization of chromatin topology safeguards genome
565 integrity. Nature *574*, 571–574.

566 Pastushenko, I., Brisebarre, A., Sifrim, A., Fioramonti, M., Revenco, T., Boumahdi, S., Van Keymeulen,
567 A., Brown, D., Moers, V., Lemaire, S., et al. (2018). Identification of the tumour transition states
568 occurring during EMT. Nature *556*, 463–468.

569 Pei, Y.-F., Liu, J., Cheng, J., Wu, W.-D., and Liu, X.-Q. (2019). Silencing of LAMC2 Reverses Epithelial-
570 Mesenchymal Transition and Inhibits Angiogenesis in Cholangiocarcinoma via Inactivation of the
571 Epidermal Growth Factor Receptor Signaling Pathway. Am. J. Pathol. *189*, 1637–1653.

572 Pellinen, T., Blom, S., Sánchez, S., Välimäki, K., Mpindi, J.-P., Azegrouz, H., Strippoli, R., Nieto, R.,
573 Vitón, M., Palacios, I., et al. (2018). ITGB1-dependent upregulation of Caveolin-1 switches TGFβ
574 signalling from tumour-suppressive to oncogenic in prostate cancer. Sci. Rep. *8*, 1–14.

575 Puram, S.V., Parikh, A.S., and Tirosh, I. (2018). Single cell RNA-seq highlights a role for a partial EMT
576 in head and neck cancer. Mol. Cell. Oncol. *5*, e1448244.

577 Ramilowski, J.A., Goldberg, T., Harshbarger, J., Kloppmann, E., Lizio, M., Satagopam, V.P., Itoh, M.,
578 Kawaji, H., Carninci, P., Rost, B., et al. (2015). A draft network of ligand–receptor-mediated
579 multicellular signalling in human. Nat. Commun. *6*, 1–12.

580 Riemondy, K.A., Jansing, N.L., Jiang, P., Redente, E.F., Gillen, A.E., Fu, R., Miller, A.J., Spence, J.R.,
581 Gerber, A.N., Hesselberth, J.R., et al. (2019). Single-cell RNA sequencing identifies TGF-β as a key
582 regenerative cue following LPS-induced lung injury. JCI Insight *4*, e123637.

583 Sadej, R., Romanska, H., Kavanagh, D., Baldwin, G., Takahashi, T., Kalia, N., and Berditchevski, F.
584 (2010). Tetraspanin CD151 Regulates Transforming Growth Factor β Signaling: Implication in
585 Tumor Metastasis. Cancer Res. *70*, 6059–6070.

586 Santibáñez, J.F., Kocić, J., Fabra, A., Cano, A., and Quintanilla, M. (2010). Rac1 modulates TGF-β1-
587 mediated epithelial cell plasticity and MMP9 production in transformed keratinocytes. FEBS Lett.
588 *584*, 2305–2310.

589 Scheel, C., Eaton, E.N., Li, S.H.-J., Chaffer, C.L., Reinhardt, F., Kah, K.-J., Bell, G., Guo, W., Rubin, J.,
590 Richardson, A.L., et al. (2011). Paracrine and Autocrine Signals Induce and Maintain Mesenchymal
591 and Stem Cell States in the Breast. Cell *145*, 926–940.

592 Sha, Y., Haensel, D., Gutierrez, G., Du, H., Dai, X., and Nie, Q. (2019). Intermediate cell states in
593 epithelial-to-mesenchymal transition. Phys. Biol. *16*, 021001.

594 Shirakihara, T., Kawasaki, T., Fukagawa, A., Semba, K., Sakai, R., Miyazono, K., Miyazawa, K., and
595 Saitoh, M. (2013). Identification of integrin α3 as a molecular marker of cells undergoing epithelial-
596 mesenchymal transition and of cancer cells with aggressive phenotypes. Cancer Sci. *104*, 1189–
597 1197.

598 Sigston, E.A.W., and Williams, B.R.G. (2017). An Emergence Framework of Carcinogenesis. Front.
599 Oncol. *7*.

600 Song, J., Wang, W., Wang, Y., Qin, Y., Wang, Y., Zhou, J., Wang, X., Zhang, Y., and Wang, Q. (2019).
601 Epithelial-mesenchymal transition markers screened in a cell-based model and validated in lung
602 adenocarcinoma. BMC Cancer *19*, 680.

603 Tabassum, D.P., and Polyak, K. (2015). Tumorigenesis: it takes a village. Nat. Rev. Cancer *15*, 473–
604 483.

605 Tallima, H., and El Ridi, R. (2018). Arachidonic acid: Physiological roles and potential health benefits
606 – A review. J. Adv. Res. *11*, 33–41.

607 Tam, W.L., Lu, H., Buikhuisen, J., Soh, B.S., Lim, E., Reinhardt, F., Wu, Z.J., Krall, J.A., Bierie, B., Guo, W.,
608 et al. (2013). Protein Kinase C α Is a Central Signaling Node and Therapeutic Target for Breast
609 Cancer Stem Cells. Cancer Cell *24*, 347–364.

610 Tamayo, P., Slonim, D., Mesirov, J., Zhu, Q., Kitareewan, S., Dmitrovsky, E., Lander, E.S., and Golub,
611 T.R. (1999). Interpreting patterns of gene expression with self-organizing maps: Methods and
612 application to hematopoietic differentiation. Proc. Natl. Acad. Sci. *96*, 2907–2912.

613 Thomson, T.M., Balcells, C., and Cascante, M. (2019). Metabolic Plasticity and Epithelial-
614 Mesenchymal Transition. J. Clin. Med. *8*, 967.

615 Tominaga, K., Minato, H., Murayama, T., Sasahara, A., Nishimura, T., Kiyokawa, E., Kanauchi, H.,
616 Shimizu, S., Sato, A., Nishioka, K., et al. (2019). Semaphorin signaling via MICAL3 induces symmetric
617 cell division to expand breast cancer stem-like cells. Proc. Natl. Acad. Sci. *116*, 625–630.

618 Ulgen, E., Ozisik, O., and Sezerman, O.U. (2019). pathfindR: An R Package for Comprehensive
619 Identification of Enriched Pathways in Omics Data Through Active Subnetworks. Front. Genet. *10*.

620 Ungefroren, H., Witte, D., and Lehnert, H. (2018). The role of small GTPases of the Rho/Rac family in
621 TGF-β-induced EMT and cell motility in cancer. Dev. Dyn. *247*, 451–461.

622 Wang, H., Meyer, C.A., Fei, T., Wang, G., Zhang, F., and Liu, X.S. (2013). A systematic approach
623 identifies FOXA1 as a key factor in the loss of epithelial traits during the epithelial-to-mesenchymal
624 transition in lung cancer. BMC Genomics *14*, 680.

625 Wei, S.C., Fattet, L., Tsai, J.H., Guo, Y., Pai, V.H., Majeski, H.E., Chen, A.C., Sah, R.L., Taylor, S.S., Engler,
626 A.J., et al. (2015). Matrix stiffness drives Epithelial-Mesenchymal Transition and tumour metastasis
627 through a TWIST1-G3BP2 mechanotransduction pathway. Nat. Cell Biol. *17*, 678–688.

628 Wirth, H., von Bergen, M., and Binder, H. (2012). Mining SOM expression portraits: feature selection
629 and integrating concepts of molecular function. BioData Min. *5*, 18.

630 Wu, C.-Y.C., Carpenter, E.S., Takeuchi, K.K., Halbrook, C.J., Peverley, L.V., Bien, H., Hall, J.C., DelGiorno,
631 K.E., Pal, D., Song, Y., et al. (2014). PI3K regulation of RAC1 is required for KRAS-induced pancreatic
632 tumorigenesis in mice. Gastroenterology *147*, 1405-1416.e7.

633 Yang, J., Antin, P., Berx, G., Blanpain, C., Brabletz, T., Bronner, M., Campbell, K., Cano, A., Casanova, J.,
634 Christofori, G., et al. (2020). Guidelines and definitions for research on epithelial–mesenchymal
635 transition. Nat. Rev. Mol. Cell Biol. 1–12.

636 Zhang, J., Tian, X.-J., Zhang, H., Teng, Y., Li, R., Bai, F., Elankumaran, S., and Xing, J. (2014). TGF-β–
637 induced epithelial-to-mesenchymal transition proceeds through stepwise activation of multiple
638 feedback loops. Sci Signal *7*, ra91–ra91.

639 Zhang, J., Lin, X., Wu, L., Huang, J.-J., Jiang, W.-Q., Kipps, T.J., and Zhang, S. (2020). Aurora B induces
640 epithelial–mesenchymal transition by stabilizing Snail1 to promote basal-like breast cancer
641 metastasis. Oncogene *39*, 2550–2567.

642 Zhang, K., Myllymäki, S.-M., Gao, P., Devarajan, R., Kytölä, V., Nykter, M., Wei, G.-H., and Manninen, A.
643 (2017). Oncogenic K-Ras upregulates ITGA6 expression via FOSL1 to induce anoikis resistance and
644 synergizes with αV-Class integrins to promote EMT. Oncogene *36*, 5681–5694.

Author contributions

Indranil Paul: Conceptualization, Methodology, Software, Data curation, Writing – Original draft, Visualization, Investigation, Formal analysis
Dante Bolzan: Software, Formal analysis
Heather Joan Hook: Investigation
Ahmed Youssef: Software
Gopal Karemore: Software
Michael Uretz John Oliphant: Investigation
Weiwei Lin: Investigation
Qian Liu: Formal analysis
Sadhna Phanse: Software
Dzmitry Padhorny: Software
Sergei Kotelnikov: Software
Carl White: Software
Andrieu Guillaume: Investigation
Pingzhao Hu: Formal analysis
Gerald Denis: Investigation
Dima Kozakov: Software
Brian Raught: Investigation
Trevor Siggers: Investigation
Stefan Wuchty: Software, Formal analysis
Senthil Muthuswamy: Conceptualization, Investigation
Andrew Emili: Conceptualization, Supervision, Writing – Original draft, Resources, Funding acquisition, Formal analysis

Acknowledgements

We dedicate our sincere gratitude to Stefano Monti, Xarelabos Varelas, Valentina Perissi and Matthew Layne for providing critical feedback on the manuscript. We thank the Microarray and Sequencing Core Facility at Boston University School of Medicine for acquisition of mRNA, miRNA and scRNAseq data.

Funding

S.M., G.D., and A.E. acknowledge joint funding (UO1CA243004) from the NCI program Research Projects in Cancer Systems Biology. The CNSB has generous ongoing support from Boston University.

Competing interests

The authors declare no competing financial interest.

Main figure legends

Figure 1. A multi-dimensional resource on TGFβ-induced EMT

(A) MCF10A cells were exposed to TGFβ for the indicated time points. A major premise of the study was to characterize various cell-states and the transition points through which EMT occurs.
(B) Samples from 3 biological replicates were aliquoted and multiple technology platforms were employed to quantify various molecular layers.
(C) An overview of numbers of molecules quantified in various layers.
(D) Expression snapshots of some well-known EMT markers. Heatmaps show log2FC values (relative to Control, FDR = 0.05).
(E) Variance explained by each layer over 4 principal components.
(F) Ridge plot showing differential molecules, as % of total quantified, for each layer.
(G) Pie chart showing the overall fraction (in %) of differential molecules (yellow portion) relative to all molecules quantified in each layer.
(H) Overlap between established EMT databases (MSigDB, www.gsea-msigdb.org; dbEMT2.0, http://dbemt.bioinfo-minzhao.org) and differential proteins and miRNAs (adj. *p-value* < 0.05; $r^2 \geq 0.6$ & $|\log2FC| \geq 1$) from this study.
(I) Differential molecules (proteins, miRNAs, metabolites) from this study were used to assess the number of coherent functional modules, i.e., biological interactions or network edges, by employing the Prize-Collecting Steiner Forest algorithm on an interaction network compiled from PathwayCommons, miRTarBase and STITCH.

Figure 2. The topological architecture of EMT

(A) Neighbor-joining was applied as a distance metric to reveal the similarities between timepoints, considering all bulk measurements, excluding *mRNA* (see text).
(B) Combined pseudo-eigenvalues space of all datasets, indicating the contribution of each dataset to the eigenvalue (variance).
(C) Matrix correlations between each pair of datasets.
(D) Line plots show the distribution of adjusted coefficient of determination (R^2) values between layers as a function of time points.
(E) *Left panel.* SOM-portraits characterizing expression landscape of the samples. Color gradient refers to over- or under-expression of metagenes (=cluster of genes) in each time-point compared to the mean expression level of the metagene in the pool of all time-points: red = high, yellow/green = intermediate levels and blue = low (see **STAR Methods** for details). *Middle panel*. Representative examples that appeared among the highest-ranking features (top 1%) in each time-point. *Right panel*. Barplot shows the number of features that were contributed by each layer among the highest-ranking features (top 1%) in time-point.
(F) Heatmap depicts sample-wise pathway scores, which were derived from subnetwork-based pathway enrichment analysis using the highest-ranking molecules (top 1%) for each SOM.

720 **Figure 3. Dynamics of TGFβ-induced metabolic adaptations**

721 (A) Barplot showing the 'class' distribution of quantified metabolite features as defined in HMBD.
722 Also shown are the relative proportions of differentially expressed features for each class (*p-*
723 *value* ≤ 0.01, absolute log2FC ≥ 1).
724 (B) Neighbor-joining tree for the *Metabol* dataset.
725 (C) SOM analysis of the *Metabol* dataset.
726 (D) Top 10% of metabolite features of each SOM were grouped based on clusters in `B` and used
727 for "Network analysis" using MetaboAnalyst (https://www.metaboanalyst.ca).
728 (E) Identified metabolites of AAM pathway in SOM for 4 hours to day 1 were taken and Pearson's
729 correlation computed with known metabolic enzymes (KEGG) quantified in the *Phos* & *Prot*
730 datasets.
731 (F) The plot shows enzymes ranked according to their Pearson's correlation with metabolites of
732 AAM pathway, as detected in this study.
733 (G) Schematics of information flow from TGFβ signaling to AAM pathway, mediated by known
734 enzymes. Heatmaps and line plots display 'standardized' expression values over the time
735 points.

736 **Figure 4. scRNAseq analysis reveals cellular dynamics and novel TFs for EMT**

737 (A) Violin plots showing expression of well-known EMT hallmarks in each time point.
738 (B) UMAP of scRNAseq by Monocle3. Dots represent single cells and are colored by inferred
739 clusters, while trajectories depict cells during EMT.
740 (C) Heatmap showing the number of cells (in log2 scale) in each cluster of partition P2. Mean
741 expression of some well-known E and M markers in each cluster are also shown.
742 (D) The plot shows all TFs ranked according to their SCENIC score. TF names are shown for the
743 5 TFs with the highest scores and some well-known EMT associated TFs.
744 (E) Tree displays unique TFs identified by SCENIC for each subtype. TFs highlighted in 'bold' are
745 known players in EMT as of dbEMT2.0. The genes in the outer circle are representative
746 examples used by SCENIC to infer TF activity.
747 (F) Barplot shows the inferred activities of top 15 TFs based on SCENIC scores in each subtype.
748 (G) Schematics of the human TF-binding array workflow (see **STAR Methods** for details).
749 (H) & (I) Density plots of ∂B-scores of indicated TFs. Two-sided Kolmogorov-Smirnov test was
750 performed to evaluate the significance of distribution differences between Control and TGFβ
751 treated conditions.

752 **Figure 5. Spatial regulation of proteins and intercellular communication**

753 (A) The schematic summarizes correlations based on Pearson's coefficients between the
754 indicated layers. Each pie chart depicts the fraction of differential proteins (orange slice) with
755 respect to all proteins quantified in the layer. The dotted lines indicate correlation of
756 overlapping proteins between layers.
757 (B) The plot displays top 25 Class I proteins. Each pair is represented by a different shape, as
758 shown.
759 (C) Expression profiles of top 3 Class I proteins. Each colored line represents a molecular layer,
760 as shown.

761 (D) The plot displays top 25 Class II proteins. Each pair is represented by a different shape, as
762 shown.
763 (E) Expression profiles of top 3 Class II proteins. Each colored line represents a molecular layer,
764 as shown.
765 (F) Expression profiles of BRD2 and BRD4 in various layers, as indicated. Legend as in E
766 (G) Density plots of ∂B-scores of indicated co-factors. Two-sided Kolmogorov-Smirnov test was
767 performed to evaluate the significance of difference in distributions.
768 (H) Phase-contrast images after 6 days of TGFβ treatment in presence or absence of active JQ-1
769 (100 nM) or its inactive analogue.
770 (I) Expression profile of SCRIB in various layers, as indicated. Legend as in E
771 (J) PPI network of SCRIB interactors identified using BioID.
772 (K) Immunoblots showing interactions of a few SCRIB partners identified using BioID.
773 (L) Schematics of analysis pipeline for discovering active L-R pairs (see **STAR Methods**).
774 (M) Heatmap showing combined log2FCs of L-R pairs in the *Sec* and *Mem/Glyco* datasets.
775 (N) Network plot showing L-R interactions detected between different P2 cell clusters.
776 (O) Scatter plot of correlations between indicated gene-pairs in Breast invasive carcinoma
777 samples. Regression line is shown in red.

778 **Figure 6. Phosphoproteome dynamics during EMT**

779 (A) Fraction of detected p-sites on a protein that are regulated during EMT.
780 (B) Detected p-sites on VIM and their expression during EMT. The gray lines indicate all p-sites
781 that are catalogued in PhosphoSitePlus database.
782 (C) Distribution of Pearson's correlation between expression of proteins and the p-sites detected
783 on them.
784 (D) Schematic showing two examples each where expression of proteins and p-sites showed
785 either low (≤–0.1; CDS2, CBX1) or high (≥0.4; MISP, MICAL3) correlation.
786 (E) Gene ontology enrichment of genes with at least a single regulated p-site at any time point.
787 (F) Distribution of Pearson's correlation between expression of proteins detected in *Nuc* layer
788 and the p-sites detected on them in the *Phos* layer. A few EMT hallmarks are highlighted.
789 (G) Heatmaps of expression profiles of indicated molecules in *Nuc* and *Phos* layers.
790 (H) Structural model of MICAL3 p-sites, NLS and Importin-α.
791 (I) Ternary plot of kinase activity scores binned into 3 broad stages of EMT, i.e., E, ICS, and M.
792 (J) *Top*. Expression of PRKCA as detected in various layers. *Bottom*. Pathway enrichment of all
793 differential substrates of PRKCA detected in our dataset.
794 (K) *Top*. Expression of AURKB as detected in various layers. *Bottom*. Pathway enrichment of all
795 differential substrates of AURKB detected in our dataset.

796 **Figure 7. Integrative systems causal model of EMT**

797 (A) Schematics of network and causal inference workflow. Non-redundant genes with most
798 significant expression (Hotelling's T^2 statistic) profiles were used for the analysis.
799 CausalPath-estimated logical networks were used to augment a custom-built confidence-
800 weighted scaffold interactome which was then used to solve the Steiner forest problem using

801 the OmicsIntegrator software. Only differential molecules (relative to Control, FDR adj.*p-*
802 *value* ≤ 0.05, |log2FC| ≥ 1) were considered as 'prizes'.
803 (B) A subgraph showing the signaling context of well-known EMT players 'queried' on the EMT
804 network.
805 (C) Kaplan-Meier plots comparing prognostic performance of MSigDB hallmarks and
806 'controllers' identified in this study, as indicated.
807 (D) Overlap between established EMT databases (as in Figure 1) and the 'controllers' identified
808 in this study.
809 (E) Overlap between the EMT databases and the 'non-controllers' identified in this study.
810 (F) A simplified schematic showing the hierarchical relationships between several bottleneck
811 genes at different stages of EMT, as indicated.
812 (G) Workflow for morphometric screening of drug combinations. The tool GENIMASEG is
813 available here: https://figshare.com/articles/software/GenImaSeg_Tool_zip/14371778
814 (H) The barplot of results of the above experiment indicates varying degrees of synergy or
815 antagonism between inhibitors, in influencing EMT-associated changes in cell shape
816 (eccentricity). Error bars indicate spread of datapoints across all quantified cells in each
817 condition.

818 Supplementary figure legends

819 **Figure S1. Related to Figure 1. A multi-dimensional resource on TGFβ-induced EMT**

820 (A) TGFβ treatments were staggered, at defined time periods, such that all plates were harvested
821 at the same time. Cells were serum starved for 16 hours before harvesting.
822 (B) Phase-contrast images of MCF10A cells at different time points. Scale bar = 100 μm.
823 (C) For maximizing efficiency while maintaining compatibility with technology-specific
824 protocols, after harvesting cells were collected in 4 aliquots per replicate, as shown.
825 Conditioned media were also collected.
826 (D) Upper panel – Barplots showing percentage of quantified proteins with annotation in the
827 'Cellular Component' category. Lower panel – Boxplots showing intensity values (log2) of
828 proteins (= markers) commonly used to assess sub-cellular fractionation purity. Box edges
829 correspond to 25th and 75th percentiles, whiskers include extreme data points.
830 (E) Cumulative distribution (%) of Pearson's coefficients across the samples (= time points).
831 Significant overlap between the 3 biological replicates, shown as 3 colors, indicates high
832 reproducibility.
833 (F) Heatmaps of molecular expression profiles of indicated layers. The mean of all quantified
834 molecules across the 3 replicates was used.
835 (G) Violin plots showing the spread of log2FCs of molecules at each time point (relative to
836 Control) for each layer.

837 **Figure S2. Related to Figure 2. The topological architecture of EMT**

838 (A) PCA of the various molecular layers. Time points are shown with different shapes and
839 colors. Points with similar shape/color indicate biological replicates.

840 (B) The population map presents the number of genes mapped to each individual metagene.
841 (C) The plot summarizes co-variance structure of datasets at the metagene level.
842 (D) The plot shows correlation of expression patterns of individual genes and the metagenes in
843 which they are contained.
844 (E) Temporal expression profiles of a few example genes identified in SOM analysis. Each colored
845 line represents a molecular layer, as shown.
846 (F) Temporal expression profiles of a few example genes enlisted as 'EMT hallmarks' in MSigDB
847 database. Each colored line represents a molecular layer, as shown.
848

849 **Figure S3. Related to Figure 3. Dynamics of TGFβ-induced metabolic adaptations**

850 (A) The heatmap displays the results of active subnetwork analysis using differential molecules
851 in *Prot* and *Phos* datasets.
852 (B) – (D) Metabolite-metabolite interaction networks, using MetaboAnalyst, for indicated
853 clusters. High connectivity indicates co-regulation of functionally related metabolites.

854 **Figure S4. Related to Figure 4. scRNAseq analysis reveals cellular dynamics and novel TFs for EMT**

855 (A) An outline of the QC pipeline employed for scRNAseq data analysis.
856 (B) The plot shows top 25 most expressed genes. Each row corresponds to a gene and each bar
857 corresponds to the expression of the gene in single cells.
858 (C) Expression of indicated genes in *mRNA* layer.
859 (D) Developmental trajectories of MCF10A cells in response to TGFβ, inferred by Monocle3.
860 Clusters are indicated by colors.
861 (E) Heatmap showing aggregate expression of groups of genes (=Modules) with similar
862 expression pattern across the *partitions*, by Monocle3. Modules 9/12 were highly expressed
863 in P1/P3 and were enriched for 'Cell cycle' related GO annotations.

864 **Figure S5. Related to Figure 5. Spatial regulation of proteins and intercellular communication**

865 (A) The plot shows number of common genes (intersection size, *y* axis) between layers as
866 indicated. Only differential genes in each layer ('Set size', FDR ≤ 0.05; adj. *p-value* ≤ 0.05; r^2 ≥
867 0.6 & |log2FC|, relative to Control, of ≥ 1) were considered for the analysis.
868 (B) Schematics of the BioID experiment performed to discover novel SCRIB partners induced by
869 TGFβ signaling.
870 (C) Circos plot showing L-R interactions between the P2 clusters.
871 (D) UMAP plots of scRNAseq data highlighting the co-expression patterns of MMP7 and CD44.

872 **Figure S6. Related to Figure 6. Phosphoproteome dynamics during EMT**

873 (A) An outline of QC pipeline for *Phos* data analysis.
874 (B) Enrichment efficiency for TiO_2 workflow employed for the study.
875 (C) About 74% of all detected p-sites were reliably localized (=Class I) by MaxQuant.
876 (D) Quantifications of p-sites were achieved with a dynamic range of 10^6 orders of magnitude.
877 (E) Proportions of number of phosphate moieties in each detected p-site.
878 (F) Number of phosphoproteins regulated over the time course.

(G) Magnitudes of log2FC values for p-sites over the time course.

(H) The plot shows all kinases ranked according to their KSEA enrichment. Mean of |z-score| values over all time points were taken.

Figure S7. Related to Figure 7. Integrative systems causal model of EMT

(A) A snapshot of the companion website which can be interactively and freely accessed at (https://srphanse.shinyapps.io/EMTAPP_2/).

Figure 1

A Experimental design and premise

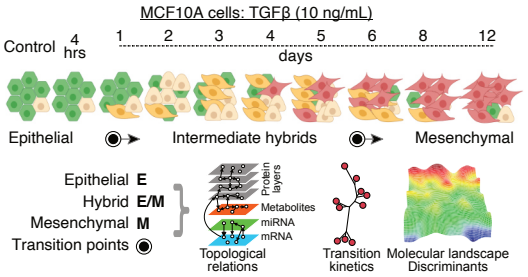

B Data acquisition, technologies and platforms

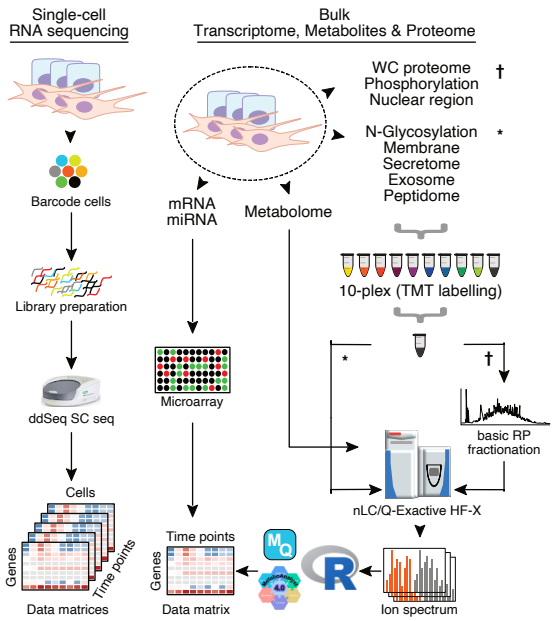

C Datasets (this study, 10 time points)

Proteomics

Component	Peptides	Genes (signif. up/dn) **	PTM sites * (signif. up/dn) **
Whole cell proteome (WC)	552,716	6,540 (403/470)	--
Nuclear region (Nuc)	286,162	4,198 (298/259)	--
Membrane (Mem)	35,870	2,223 (149/131)	--
Peptidome (Pep)	735	202 (31/31)	--
Secretome (Sec)	27,136	1,133 (247/200)	--
Extracellular vesicles (EV)	20,438	1,209 (149/123)	--
Glycosylated proteins (Glyco)	6696	590 (17/26)	--
Phosphorylation (Phos)	149,469	2,254	8,741 (1,536/1,602)
Total unique proteins	--	7,632	--

Transcriptomics

Single cell	Matrix	Total RNA	Genes (signif. up/dn)
Number of cells ***	1,913	mRNA	23,787 (2,441/1,993)
mRNA	9,785	mi-RNA	2,574 (178/118)

Metabolomics

	Features (MS1 peaks)	HMDB indexed	KEGG indexed
Features (Level 2) ****	27,759	8,325 (610/468)	1,118 (65/59)

* Unique PTM sites remaining after QC steps; ** relative to `Control`; absolute log2FC ≥ 1, FDR ≤ 0.05, r^2 ≥ 0.6;
*** Number of cells & genes remaining after QC steps **** Level 2 identifications (Salek et al., 2013)

D MultiOmic profiles of EMT markers

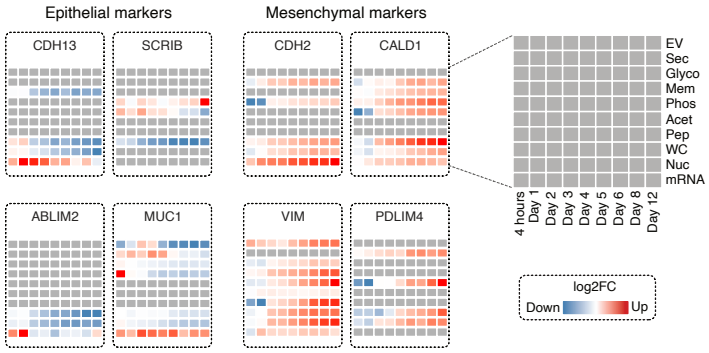

E Variance contribution

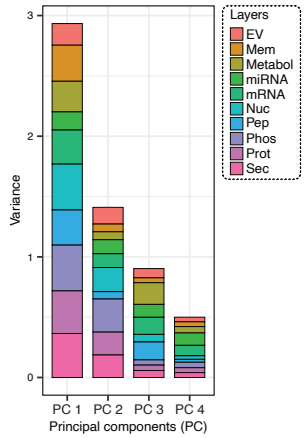

F Differential molecules over time points

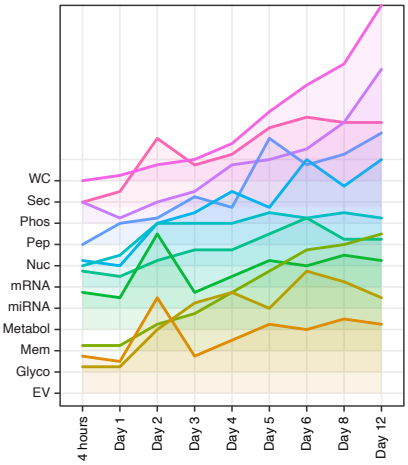

G Differential molecules as % of total detected

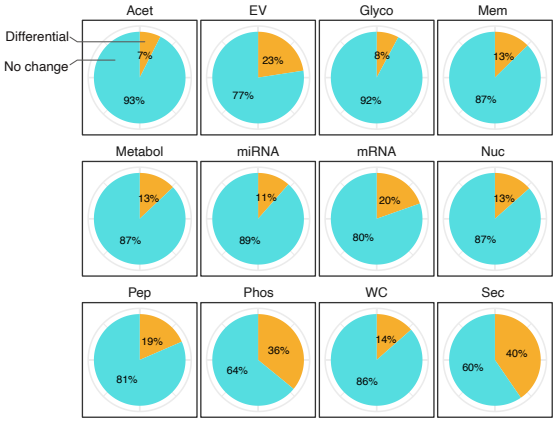

H Comparison to current knowledge

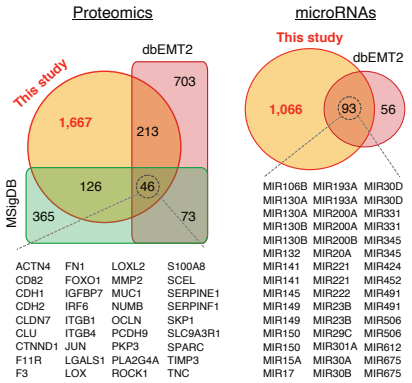

I Enhanced discovery of coherent functional modules

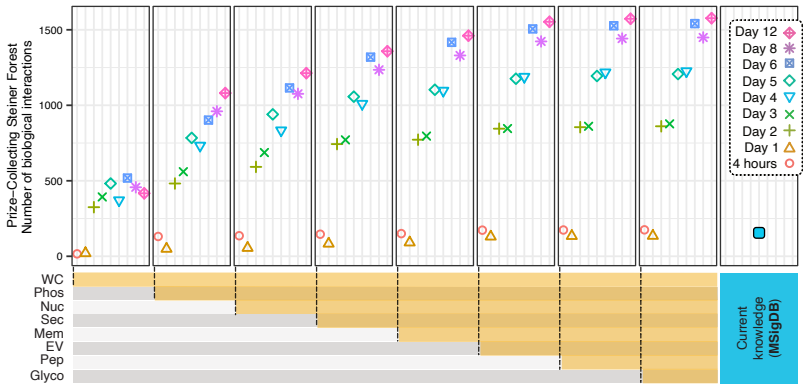

Figure 2

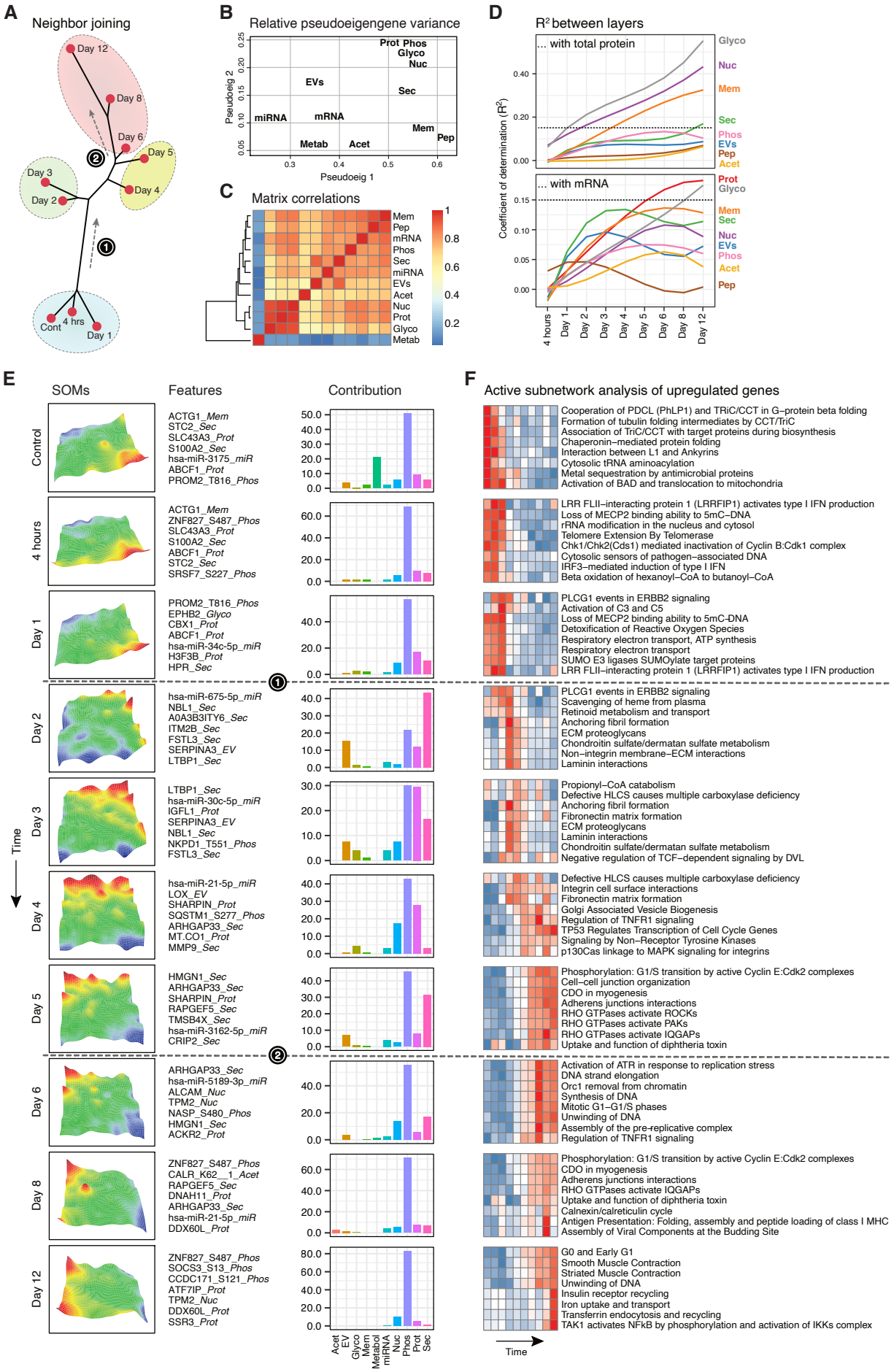
A
Neighbor joining
Day 12
Day 8
Day 6
Day 5
Day 4
Day 3
Day 2
Cont
4 hrs
Day 1
B
Relative pseudoeigengene variance
Pseudoeig 2
Pseudoeig 1
Prot Phos
Glyco
Nuc
EVs
Sec
miRNA
mRNA
Mem
Pep
Metab
Acet
C
Matrix correlations
Mem
Pep
mRNA
Phos
Sec
miRNA
EVs
Acet
Nuc
Prot
Glyco
Metab
D
R² between layers
... with total protein
... with mRNA
Coefficient of determination (R²)
Glyco
Nuc
Mem
Sec
Phos
EVs
Pep
Acet
Prot
4 hours
Day 1
Day 2
Day 3
Day 4
Day 5
Day 6
Day 8
Day 12
E
SOMs
Features
Contribution
Control
4 hours
Day 1
Day 2
Day 3
Day 4
Day 5
Day 6
Day 8
Day 12
Time
ACTG1_Mem
STC2_Sec
SLC43A3_Prot
S100A2_Sec
hsa-miR-3175_miR
ABCF1_Prot
PROM2_T816_Phos
ACTG1_Mem
ZNF827_S487_Phos
SLC43A3_Prot
S100A2_Sec
ABCF1_Prot
STC2_Sec
SRSF7_S227_Phos
PROM2_T816_Phos
EPHB2_Glyco
CBX1_Prot
ABCF1_Prot
hsa-miR-34c-5p_miR
H3F3B_Prot
HPR_Sec
hsa-miR-675-5p_miR
NBL1_Sec
A0A3B3ITY6_Sec
ITM2B_Sec
FSTL3_Sec
SERPINA3_EV
LTBP1_Sec
LTBP1_Sec
hsa-miR-30c-5p_miR
IGFL1_Prot
SERPINA3_EV
NBL1_Sec
NKPD1_T551_Phos
FSTL3_Sec
hsa-miR-21-5p_miR
LOX_EV
SHARPIN_Prot
SQSTM1_S277_Phos
ARHGAP33_Sec
MT.CO1_Prot
MMP9_Sec
HMGN1_Sec
ARHGAP33_Sec
SHARPIN_Prot
RAPGEF5_Sec
TMSB4X_Sec
hsa-miR-3162-5p_miR
CRIP2_Sec
ARHGAP33_Sec
hsa-miR-5189-3p_miR
ALCAM_Nuc
TPM2_Nuc
NASP_S480_Phos
HMGN1_Sec
ACKR2_Prot
ZNF827_S487_Phos
CALR_K62__1_Acet
RAPGEF5_Sec
DNAH11_Prot
ARHGAP33_Sec
hsa-miR-21-5p_miR
DDX60L_Prot
ZNF827_S487_Phos
SOCS3_S13_Phos
CCDC171_S121_Phos
ATF7IP_Prot
TPM2_Nuc
DDX60L_Prot
SSR3_Prot
Acet
EV
Glyco
Mem
Metabol
miRNA
Nuc
Phos
Prot
Sec
F
Active subnetwork analysis of upregulated genes
Cooperation of PDCL (PhLP1) and TRiC/CCT in G–protein beta folding
Formation of tubulin folding intermediates by CCT/TriC
Association of TriC/CCT with target proteins during biosynthesis
Chaperonin–mediated protein folding
Interaction between L1 and Ankyrins
Cytosolic tRNA aminoacylation
Metal sequestration by antimicrobial proteins
Activation of BAD and translocation to mitochondria
LRR FLII–interacting protein 1 (LRRFIP1) activates type I IFN production
Loss of MECP2 binding ability to 5mC–DNA
rRNA modification in the nucleus and cytosol
Telomere Extension By Telomerase
Chk1/Chk2(Cds1) mediated inactivation of Cyclin B:Cdk1 complex
Cytosolic sensors of pathogen–associated DNA
IRF3–mediated induction of type I IFN
Beta oxidation of hexanoyl–CoA to butanoyl–CoA
PLCG1 events in ERBB2 signaling
Activation of C3 and C5
Loss of MECP2 binding ability to 5mC-DNA
Detoxification of Reactive Oxygen Species
Respiratory electron transport, ATP synthesis
Respiratory electron transport
SUMO E3 ligases SUMOylate target proteins
LRR FLII–interacting protein 1 (LRRFIP1) activates type I IFN production
PLCG1 events in ERBB2 signaling
Scavenging of heme from plasma
Retinoid metabolism and transport
Anchoring fibril formation
ECM proteoglycans
Chondroitin sulfate/dermatan sulfate metabolism
Non–integrin membrane–ECM interactions
Laminin interactions
Propionyl–CoA catabolism
Defective HLCS causes multiple carboxylase deficiency
Anchoring fibril formation
Fibronectin matrix formation
ECM proteoglycans
Laminin interactions
Chondroitin sulfate/dermatan sulfate metabolism
Negative regulation of TCF–dependent signaling by DVL
Defective HLCS causes multiple carboxylase deficiency
Integrin cell surface interactions
Fibronectin matrix formation
Golgi Associated Vesicle Biogenesis
Regulation of TNFR1 signaling
TP53 Regulates Transcription of Cell Cycle Genes
Signaling by Non–Receptor Tyrosine Kinases
p130Cas linkage to MAPK signaling for integrins
Phosphorylation: G1/S transition by active Cyclin E:Cdk2 complexes
Cell–cell junction organization
CDO in myogenesis
Adherens junctions interactions
RHO GTPases activate ROCKs
RHO GTPases activate PAKs
RHO GTPases activate IQGAPs
Uptake and function of diphtheria toxin
Activation of ATR in response to replication stress
DNA strand elongation
Orc1 removal from chromatin
Synthesis of DNA
Mitotic G1–G1/S phases
Unwinding of DNA
Assembly of the pre-replicative complex
Regulation of TNFR1 signaling
Phosphorylation: G1/S transition by active Cyclin E:Cdk2 complexes
CDO in myogenesis
Adherens junctions interactions
RHO GTPases activate IQGAPs
Uptake and function of diphtheria toxin
Calnexin/calreticulin cycle
Antigen Presentation: Folding, assembly and peptide loading of class I MHC
Assembly of Viral Components at the Budding Site
G0 and Early G1
Smooth Muscle Contraction
Striated Muscle Contraction
Unwinding of DNA
Insulin receptor recycling
Iron uptake and transport
Transferrin endocytosis and recycling
TAK1 activates NFkB by phosphorylation and activation of IKKs complex
Time

Figure 3

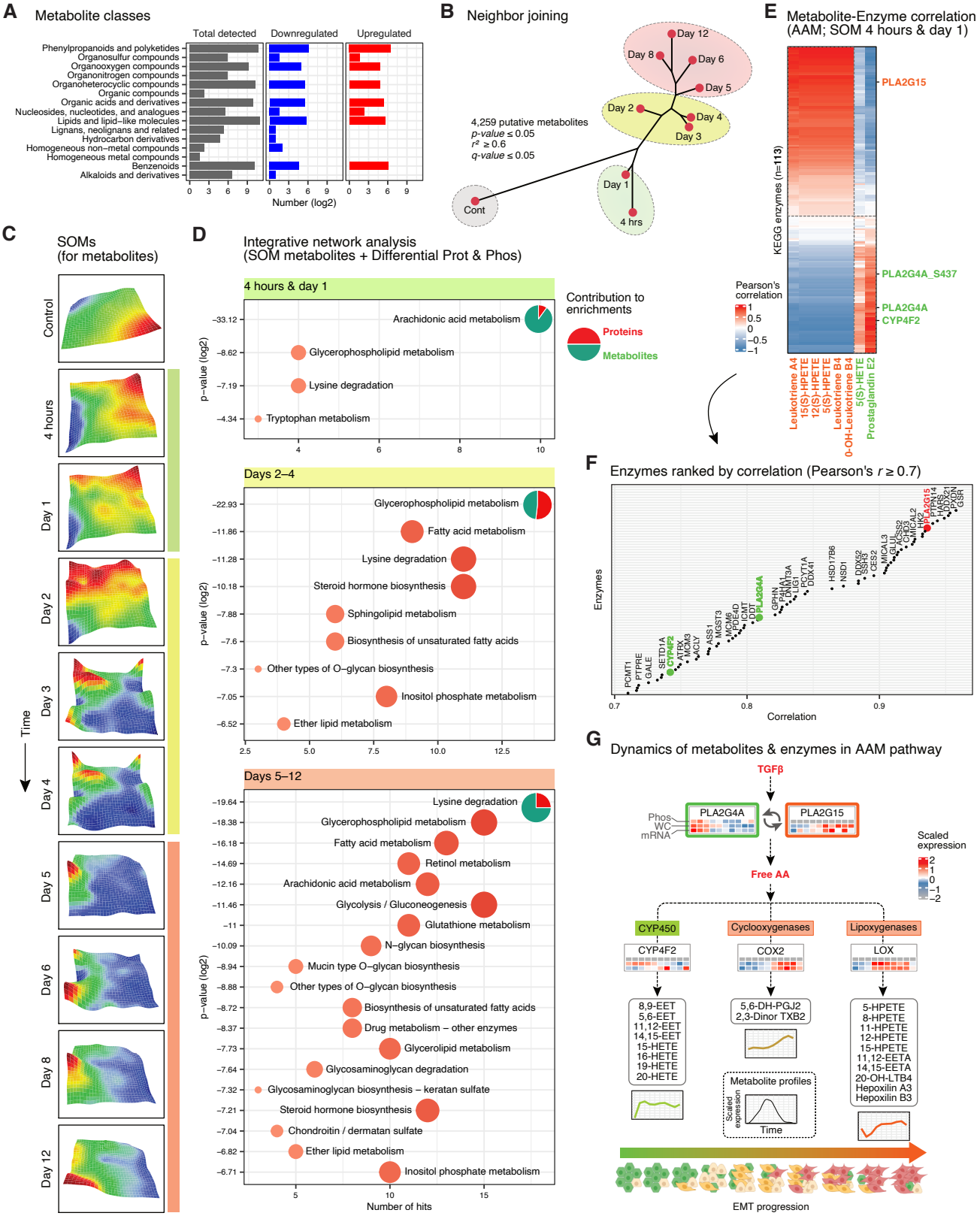
A
Metabolite classes
Total detected
Downregulated
Upregulated
Phenylpropanoids and polyketides
Organosulfur compounds
Organooxygen compounds
Organonitrogen compounds
Organoheterocyclic compounds
Organic compounds
Organic acids and derivatives
Nucleosides, nucleotides, and analogues
Lipids and lipid–like molecules
Lignans, neolignans and related
Hydrocarbon derivatives
Homogeneous non–metal compounds
Homogeneous metal compounds
Benzenoids
Alkaloids and derivatives
Number (log2)
B
Neighbor joining
4,259 putative metabolites
p-value ≤ 0.05
r² ≥ 0.6
q-value ≤ 0.05
Day 12
Day 8
Day 6
Day 5
Day 2
Day 4
Day 3
Day 1
4 hrs
Cont
C
SOMs
(for metabolites)
Control
4 hours
Day 1
Day 2
Day 3
Day 4
Day 5
Day 6
Day 8
Day 12
Time
D
Integrative network analysis
(SOM metabolites + Differential Prot & Phos)
4 hours & day 1
Arachidonic acid metabolism
Glycerophospholipid metabolism
Lysine degradation
Tryptophan metabolism
Days 2–4
Glycerophospholipid metabolism
Fatty acid metabolism
Lysine degradation
Steroid hormone biosynthesis
Sphingolipid metabolism
Biosynthesis of unsaturated fatty acids
Other types of O–glycan biosynthesis
Inositol phosphate metabolism
Ether lipid metabolism
Days 5–12
Lysine degradation
Glycerophospholipid metabolism
Fatty acid metabolism
Retinol metabolism
Arachidonic acid metabolism
Glycolysis / Gluconeogenesis
Glutathione metabolism
N–glycan biosynthesis
Mucin type O–glycan biosynthesis
Other types of O–glycan biosynthesis
Biosynthesis of unsaturated fatty acids
Drug metabolism – other enzymes
Glycerolipid metabolism
Glycosaminoglycan degradation
Glycosaminoglycan biosynthesis – keratan sulfate
Steroid hormone biosynthesis
Chondroitin / dermatan sulfate
Ether lipid metabolism
Inositol phosphate metabolism
p–value (log2)
Number of hits
Contribution to enrichments
Proteins
Metabolites
E
Metabolite-Enzyme correlation
(AAM; SOM 4 hours & day 1)
KEGG enzymes (n=113)
PLA2G15
PLA2G4A_S437
PLA2G4A
CYP4F2
Pearson's correlation
Leukotriene A4
15(S)-HPETE
12(S)-HPETE
5(S)-HPETE
Leukotriene B4
0-OH-Leukotriene B4
5(S)-HETE
Prostaglandin E2
F
Enzymes ranked by correlation (Pearson's r ≥ 0.7)
Enzymes
Correlation
G
Dynamics of metabolites & enzymes in AAM pathway
TGFβ
Phos
WC
mRNA
PLA2G4A
PLA2G15
Scaled expression
Free AA
CYP450
Cyclooxygenases
Lipoxygenases
CYP4F2
COX2
LOX
8,9-EET
5,6-EET
11,12-EET
14,15-EET
15-HETE
16-HETE
19-HETE
20-HETE
5,6-DH-PGJ2
2,3-Dinor TXB2
5-HPETE
8-HPETE
11-HPETE
12-HPETE
15-HPETE
11,12-EETA
14,15-EETA
20-OH-LTB4
Hepoxilin A3
Hepoxilin B3
Metabolite profiles
Scaled expression
Time
EMT progression

Figure 4

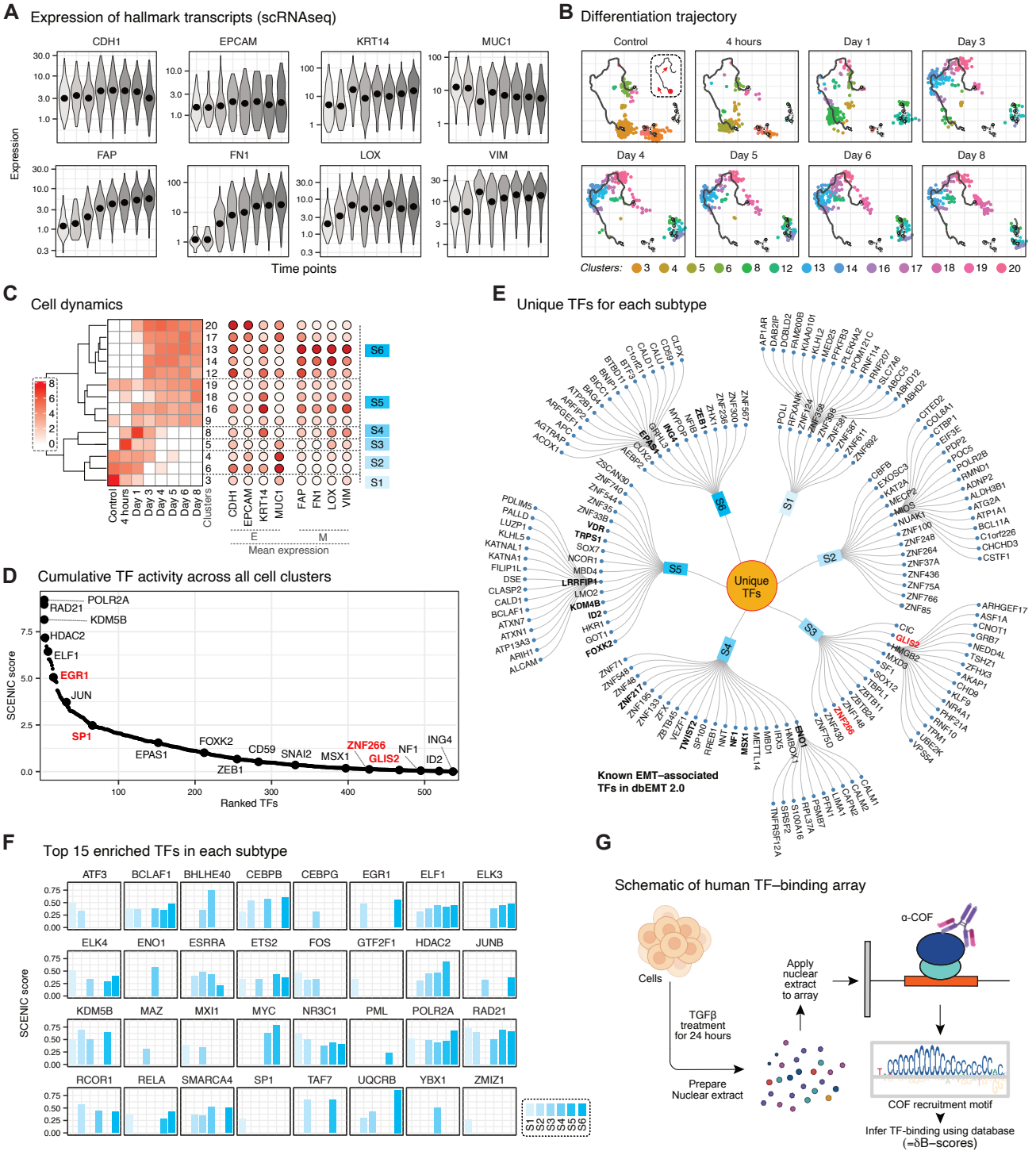
A
Expression of hallmark transcripts (scRNAseq)
CDH1
EPCAM
KRT14
MUC1
FAP
FN1
LOX
VIM
Expression
Time points
B
Differentiation trajectory
Control
4 hours
Day 1
Day 3
Day 4
Day 5
Day 6
Day 8
Clusters: 3 4 5 6 8 12 13 14 16 17 18 19 20
C
Cell dynamics
Clusters
Mean expression
D
Cumulative TF activity across all cell clusters
SCENIC score
Ranked TFs
POLR2A
RAD21
KDM5B
HDAC2
ELF1
EGR1
JUN
SP1
EPAS1
FOXK2
ZEB1
CD59
SNAI2
MSX1
ZNF266
GLIS2
NF1
ING4
ID2
E
Unique TFs for each subtype
Unique TFs
S1
S2
S3
S4
S5
S6
Known EMT–associated TFs in dbEMT 2.0
F
Top 15 enriched TFs in each subtype
SCENIC score
ATF3
BCLAF1
BHLHE40
CEBPB
CEBPG
EGR1
ELF1
ELK3
ELK4
ENO1
ESRRA
ETS2
FOS
GTF2F1
HDAC2
JUNB
KDM5B
MAZ
MXI1
MYC
NR3C1
PML
POLR2A
RAD21
RCOR1
RELA
SMARCA4
SP1
TAF7
UQCRB
YBX1
ZMIZ1
G
Schematic of human TF–binding array
Cells
TGFβ treatment for 24 hours
Prepare Nuclear extract
Apply nuclear extract to array
α-COF
COF recruitment motif
Infer TF-binding using database (=δB–scores)
H
δB–score distributions
Transcription factors
ZNF263
SP1
GLIS2
δB–scores
Recovered
Consensus
I
δB–score distributions
Transcription factors
PAX1
GCM2
EGR1
δB–scores
Recovered
Consensus

Figure 5

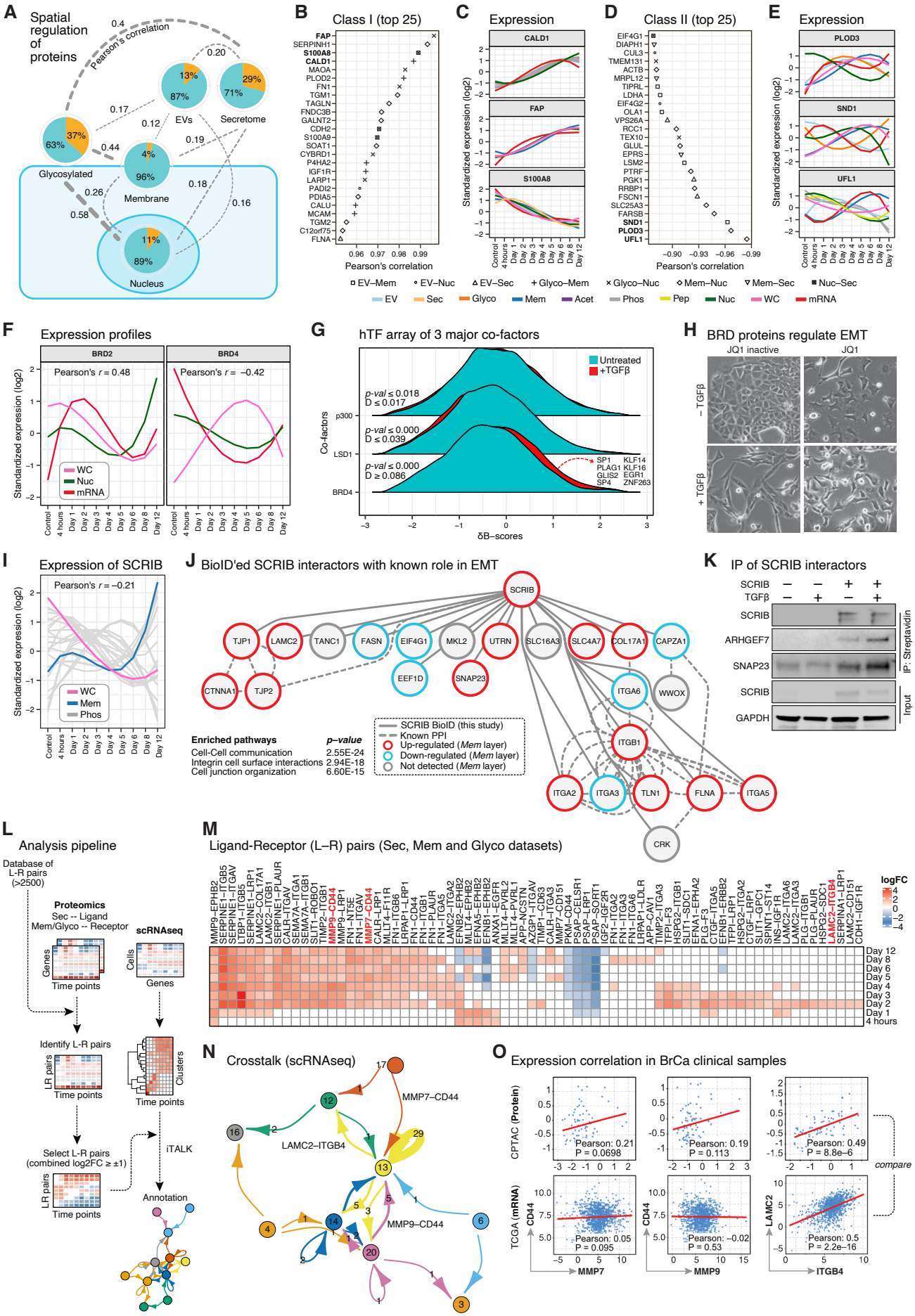
A
Spatial regulation of proteins
Pearson's correlation
EVs
Secretome
Glycosylated
Membrane
Nucleus
B
Class I (top 25)
Pearson's correlation
C
Expression
CALD1
FAP
S100A8
Standardized expression (log2)
D
Class II (top 25)
Pearson's correlation
E
Expression
PLOD3
SND1
UFL1
EV–Mem
EV–Nuc
EV–Sec
Glyco–Mem
Glyco–Nuc
Mem–Nuc
Mem–Sec
Nuc–Sec
EV
Sec
Glyco
Mem
Acet
Phos
Pep
Nuc
WC
mRNA
F
Expression profiles
BRD2
BRD4
Pearson's r = 0.48
Pearson's r = −0.42
WC
Nuc
mRNA
G
hTF array of 3 major co-factors
Untreated
+TGFβ
Co-factors
p300
LSD1
BRD4
δB–scores
H
BRD proteins regulate EMT
JQ1 inactive
JQ1
– TGFβ
+ TGFβ
I
Expression of SCRIB
Pearson's r = −0.21
WC
Mem
Phos
J
BioID'ed SCRIB interactors with known role in EMT
SCRIB
TJP1
LAMC2
TANC1
FASN
EIF4G1
MKL2
UTRN
SLC16A3
SLC4A7
COL17A1
CAPZA1
CTNNA1
TJP2
EEF1D
SNAP23
ITGA6
WWOX
ITGB1
ITGA2
ITGA3
TLN1
FLNA
ITGA5
CRK
Enriched pathways
p–value
Cell-Cell communication 2.55E-24
Integrin cell surface interactions 2.94E-18
Cell junction organization 6.60E-15
SCRIB BioID (this study)
Known PPI
Up-regulated (Mem layer)
Down-regulated (Mem layer)
Not detected (Mem layer)
K
IP of SCRIB interactors
SCRIB
TGFβ
ARHGEF7
SNAP23
GAPDH
IP: Streptavidin
Input
L
Analysis pipeline
Database of L-R pairs (>2500)
Proteomics
Sec -- Ligand
Mem/Glyco -- Receptor
scRNAseq
Genes
Time points
Cells
Identify L-R pairs
LR pairs
Clusters
Select L-R pairs (combined log2FC ≥ ±1)
iTALK
Annotation
M
Ligand-Receptor (L–R) pairs (Sec, Mem and Glyco datasets)
logFC
Day 12
Day 8
Day 6
Day 5
Day 4
Day 3
Day 2
Day 1
4 hours
N
Crosstalk (scRNAseq)
MMP7–CD44
LAMC2–ITGB4
MMP9–CD44
O
Expression correlation in BrCa clinical samples
CPTAC (Protein)
TCGA (mRNA)
Pearson: 0.21
P = 0.0698
Pearson: 0.19
P = 0.113
Pearson: 0.49
P = 8.8e−6
Pearson: 0.05
P = 0.095
Pearson: −0.02
P = 0.53
Pearson: 0.5
P = 2.2e−16
compare
CD44
LAMC2
MMP7
MMP9
ITGB4

Figure 6

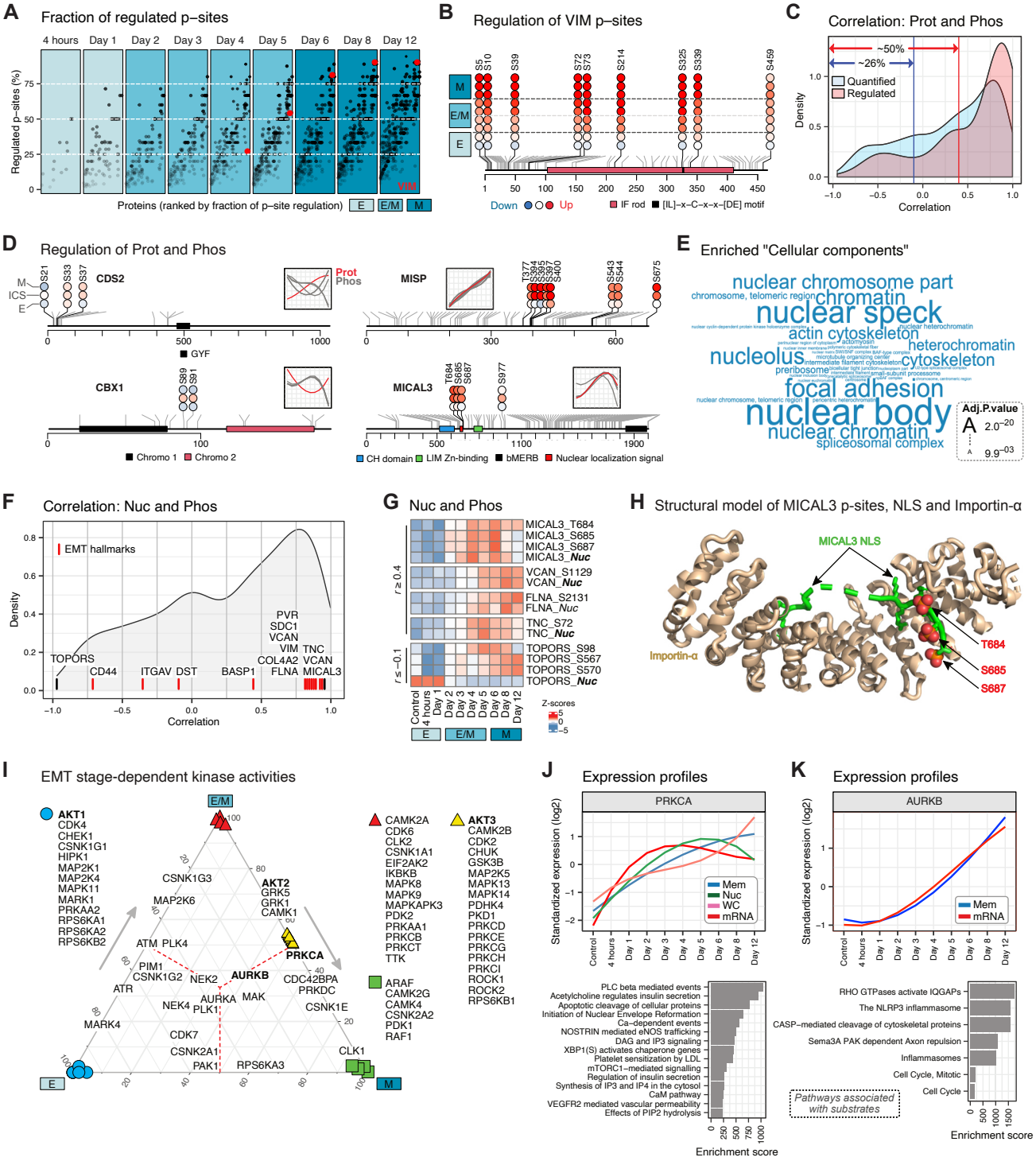
A
Fraction of regulated p–sites
4 hours
Day 1
Day 2
Day 3
Day 4
Day 5
Day 6
Day 8
Day 12
Regulated p–sites (%)
VIM
Proteins (ranked by fraction of p–site regulation)
E
E/M
M
B
Regulation of VIM p–sites
Down
Up
IF rod
[IL]–x–C–x–x–[DE] motif
C
Correlation: Prot and Phos
~50%
~26%
Quantified
Regulated
Density
Correlation
D
Regulation of Prot and Phos
CDS2
Prot
Phos
MISP
GYF
CBX1
MICAL3
Chromo 1
Chromo 2
CH domain
LIM Zn-binding
bMERB
Nuclear localization signal
E
Enriched "Cellular components"
nuclear chromosome part
chromatin
nuclear speck
actin cytoskeleton
heterochromatin
nucleolus
cytoskeleton
focal adhesion
nuclear body
nuclear chromatin
spliceosomal complex
Adj.P.value
F
Correlation: Nuc and Phos
EMT hallmarks
TOPORS
CD44
ITGAV
DST
BASP1
PVR
SDC1
VCAN
VIM
TNC
COL4A2
FLNA
MICAL3
Density
Correlation
G
Nuc and Phos
MICAL3_T684
MICAL3_S685
MICAL3_S687
MICAL3_Nuc
VCAN_S1129
VCAN_Nuc
FLNA_S2131
FLNA_Nuc
TNC_S72
TNC_Nuc
TOPORS_S98
TOPORS_S567
TOPORS_S570
TOPORS_Nuc
Z-scores
H
Structural model of MICAL3 p-sites, NLS and Importin-α
MICAL3 NLS
Importin-α
T684
S685
S687
I
EMT stage-dependent kinase activities
AKT1
CDK4
CHEK1
CSNK1G1
HIPK1
MAP2K1
MAP2K4
MAPK11
MARK1
PRKAA2
RPS6KA1
RPS6KA2
RPS6KB2
CAMK2A
CDK6
CLK2
CSNK1A1
EIF2AK2
IKBKB
MAPK8
MAPK9
MAPKAPK3
PDK2
PRKAA1
PRKCB
PRKCT
TTK
AKT3
CAMK2B
CDK2
CHUK
GSK3B
MAP2K5
MAPK13
MAPK14
PDHK4
PKD1
PRKCD
PRKCE
PRKCG
PRKCH
PRKCI
ROCK1
ROCK2
RPS6KB1
ARAF
CAMK2G
CAMK4
CSNK2A2
PDK1
RAF1
J
Expression profiles
PRKCA
Standardized expression (log2)
Mem
Nuc
WC
mRNA
PLC beta mediated events
Acetylcholine regulates insulin secretion
Apoptotic cleavage of cellular proteins
Initiation of Nuclear Envelope Reformation
Ca–dependent events
NOSTRIN mediated eNOS trafficking
DAG and IP3 signaling
XBP1(S) activates chaperone genes
Platelet sensitization by LDL
mTORC1–mediated signalling
Regulation of insulin secretion
Synthesis of IP3 and IP4 in the cytosol
CaM pathway
VEGFR2 mediated vascular permeability
Effects of PIP2 hydrolysis
Enrichment score
K
Expression profiles
AURKB
Mem
mRNA
RHO GTPases activate IQGAPs
The NLRP3 inflammasome
CASP–mediated cleavage of cytoskeletal proteins
Sema3A PAK dependent Axon repulsion
Inflammasomes
Cell Cycle, Mitotic
Cell Cycle
Pathways associated with substrates
Enrichment score

Figure 7

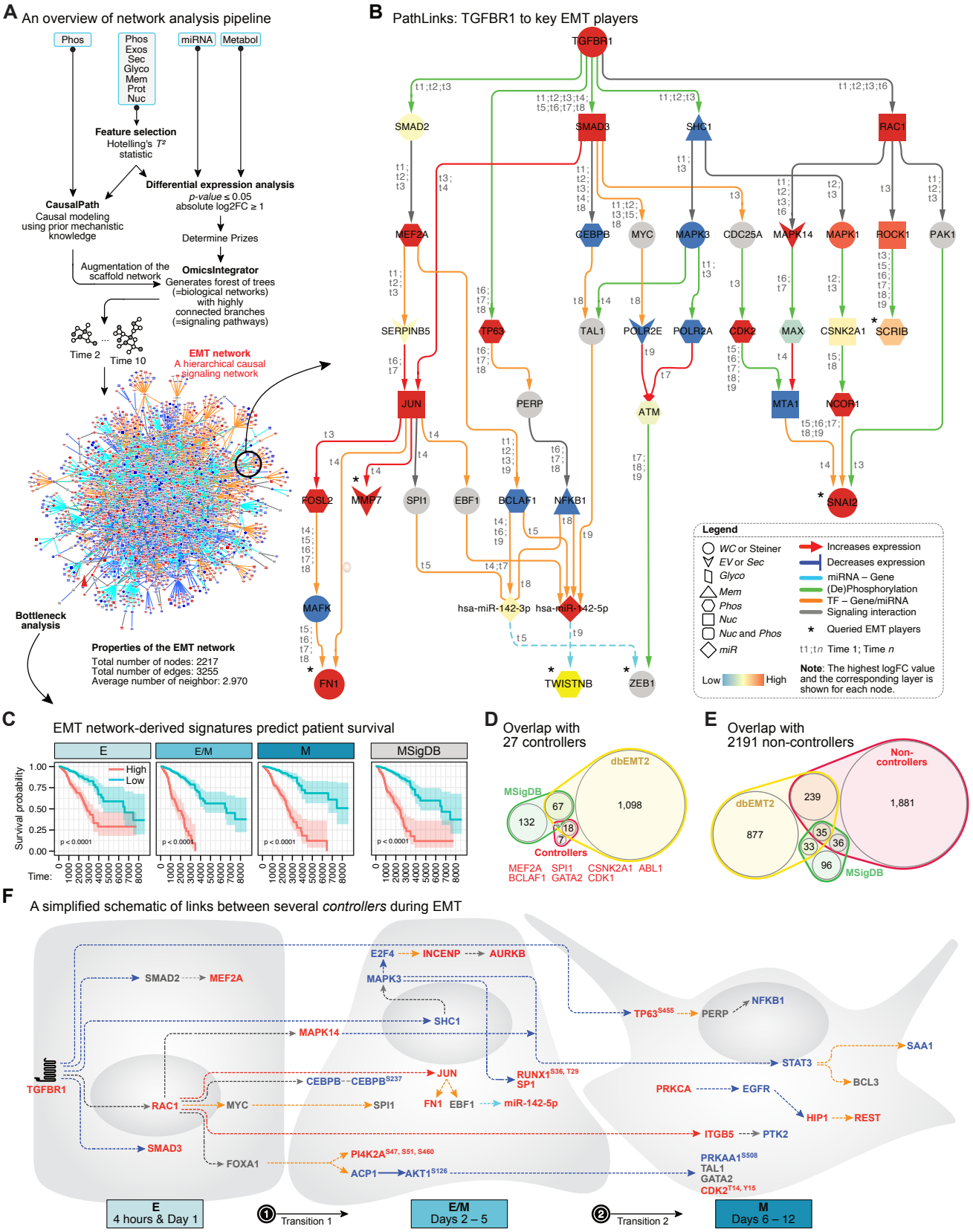
A An overview of network analysis pipeline
Phos
Phos Exos Sec Glyco Mem Prot Nuc
miRNA
Metabol
Feature selection
Hotelling's T² statistic
CausalPath
Causal modeling using prior mechanistic knowledge
Differential expression analysis
p-value ≤ 0.05
absolute log2FC ≥ 1
Determine Prizes
Augmentation of the scaffold network
OmicsIntegrator
Generates forest of trees (=biological networks) with highly connected branches (=signaling pathways)
Time 2
Time 10
EMT network
A hierarchical causal signaling network
Bottleneck analysis
Properties of the EMT network
Total number of nodes: 2217
Total number of edges: 3255
Average number of neighbor: 2.970
B PathLinks: TGFBR1 to key EMT players
TGFBR1
SMAD2
SMAD3
SHC1
RAC1
MEF2A
CEBPB
MYC
MAPK3
CDC25A
MAPK14
MAPK1
ROCK1
PAK1
SERPINB5
TP63
TAL1
POLR2E
POLR2A
CDK2
MAX
CSNK2A1
SCRIB
JUN
PERP
ATM
MTA1
NCOR1
FOSL2
MMP7
SPI1
EBF1
BCLAF1
NFKB1
SNAI2
MAFK
hsa-miR-142-3p
hsa-miR-142-5p
FN1
TWISTNB
ZEB1
Legend
WC or Steiner
EV or Sec
Glyco
Mem
Phos
Nuc
Nuc and Phos
miR
Increases expression
Decreases expression
miRNA – Gene
(De)Phosphorylation
TF – Gene/miRNA
Signaling interaction
Queried EMT players
t1;tn Time 1; Time n
Low High
Note: The highest logFC value and the corresponding layer is shown for each node.
C EMT network-derived signatures predict patient survival
E
E/M
M
MSigDB
Survival probability
High
Low
p < 0.0001
Time:
D Overlap with 27 controllers
dbEMT2
MSigDB
1,098
132
67
18
7
Controllers
MEF2A SPI1 CSNK2A1 ABL1
BCLAF1 GATA2 CDK1
E Overlap with 2191 non-controllers
Non-controllers
dbEMT2
239
1,881
877
35
33
36
96
MSigDB
F A simplified schematic of links between several controllers during EMT
E2F4
INCENP
AURKB
SMAD2
MEF2A
MAPK3
TP63S455
PERP
NFKB1
SHC1
MAPK14
STAT3
SAA1
BCL3
TGFBR1
CEBPB
CEBPBS237
JUN
RUNX1S36, T29
SP1
PRKCA
EGFR
RAC1
MYC
SPI1
FN1
EBF1
miR-142-5p
HIP1
REST
ITGB5
PTK2
SMAD3
FOXA1
PI4K2AS47, S51, S460
ACP1
AKT1S126
PRKAA1S508
TAL1
GATA2
CDK2T14, Y15
E
4 hours & Day 1
Transition 1
E/M
Days 2 – 5
Transition 2
M
Days 6 – 12
G Workflow for morphometric analysis of inhibitor screen
Controllers
Selected Inhibitors
Experiment
Analysis
Inhibitor
Target
EMT inhibitor 1
Known EMT blocker
Sonidegib
Hh inhibitor
LB-100
PP2A inhibitor
Barasertib
AURKB inhibitor
Autocamtide
CaMK-II inhibitor
PP1
SRC inhibitor
APCP
NT5E inhibitor
TGFβ
+
Inhibitor permutations
Control
Day 3
GEN IMA SEG
Generic Image Segmentation Tool
Original
Segmented
Mask
Measured: Circularity of cells
H Exposed combinatorial vulnerabilities
TGFβ/Control
EMT inhibitor 1
Sonidegib
LB-100
Barasertib
Autocamtide
PP1
APCP

Figure S1. Related to Figure 1

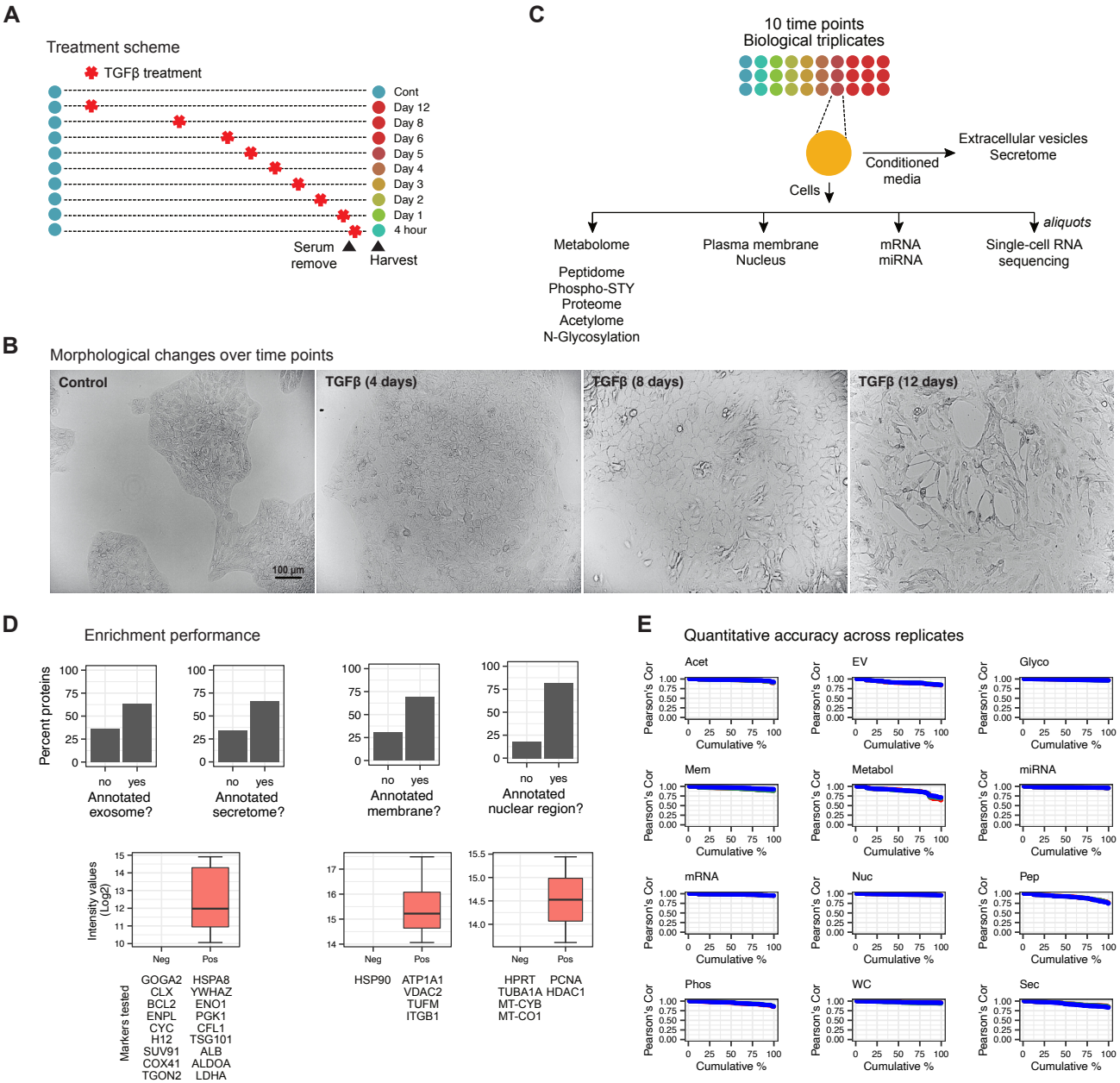

Figure S2. Related to Figure 2

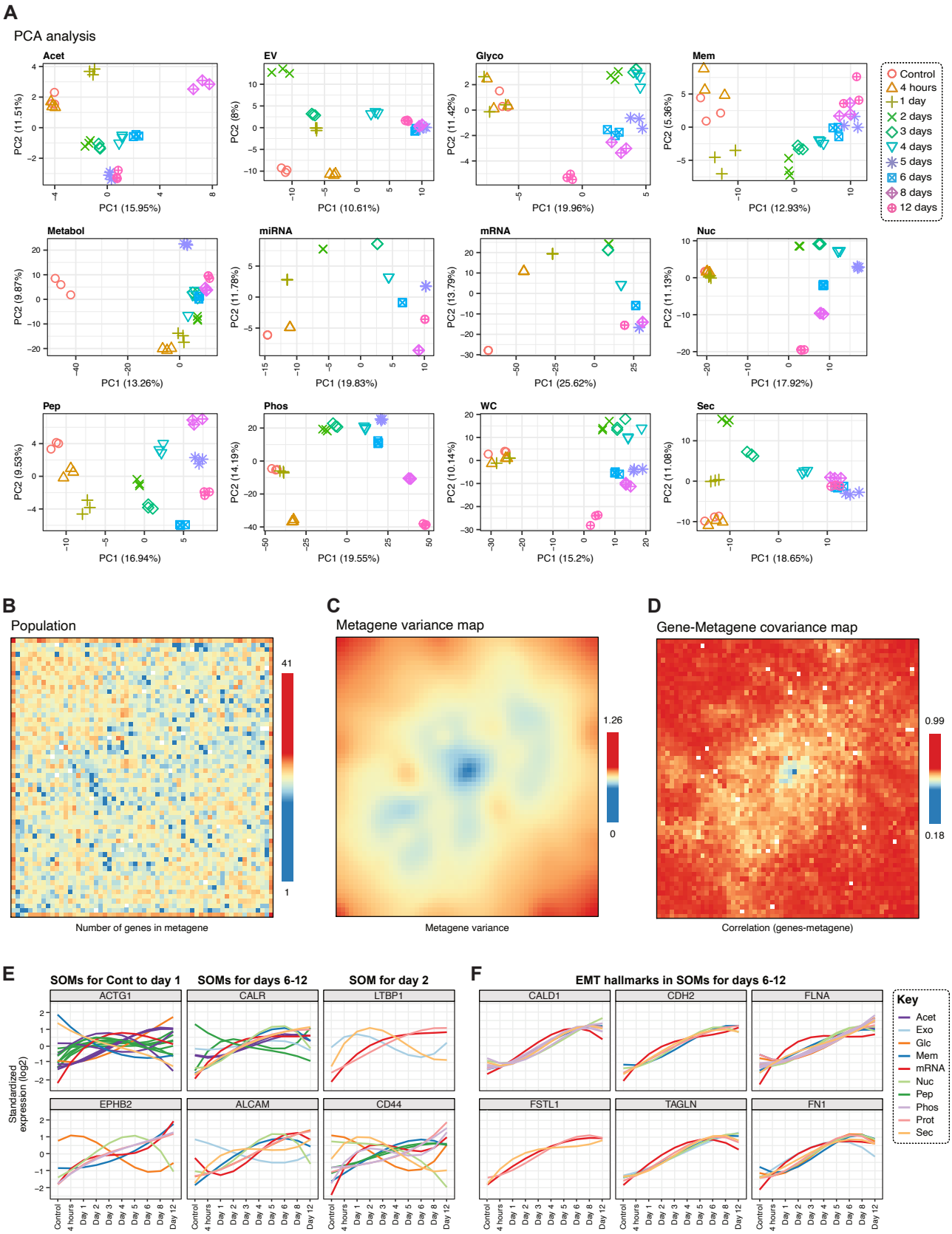

Figure S3. Related to Figure 3

A

GeneSet enrichment of metabolic pathways using active subnetworks

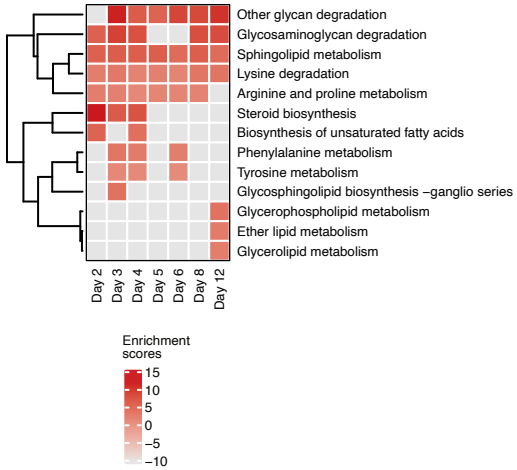

B

Metabolite-metabolite interaction network of metabolites identified in SOM for **4 hours to day 1**

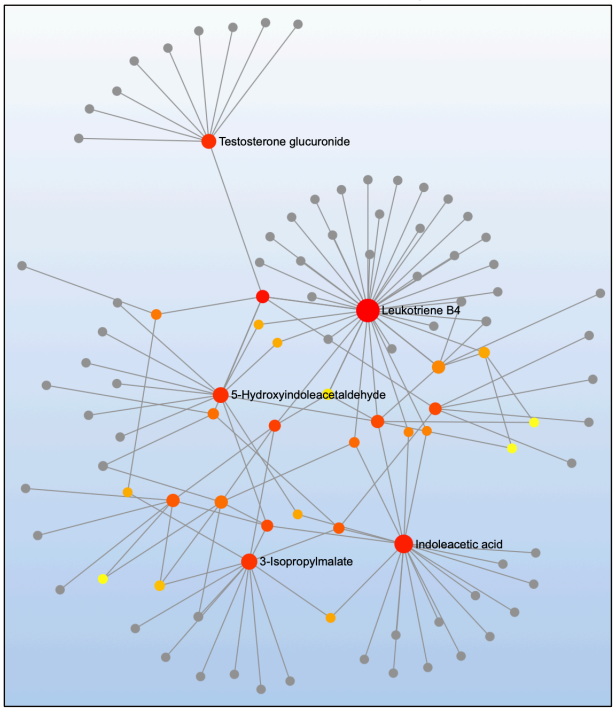

C

Metabolite-metabolite interaction network of metabolites identified in SOM for **day 2 to day 4**

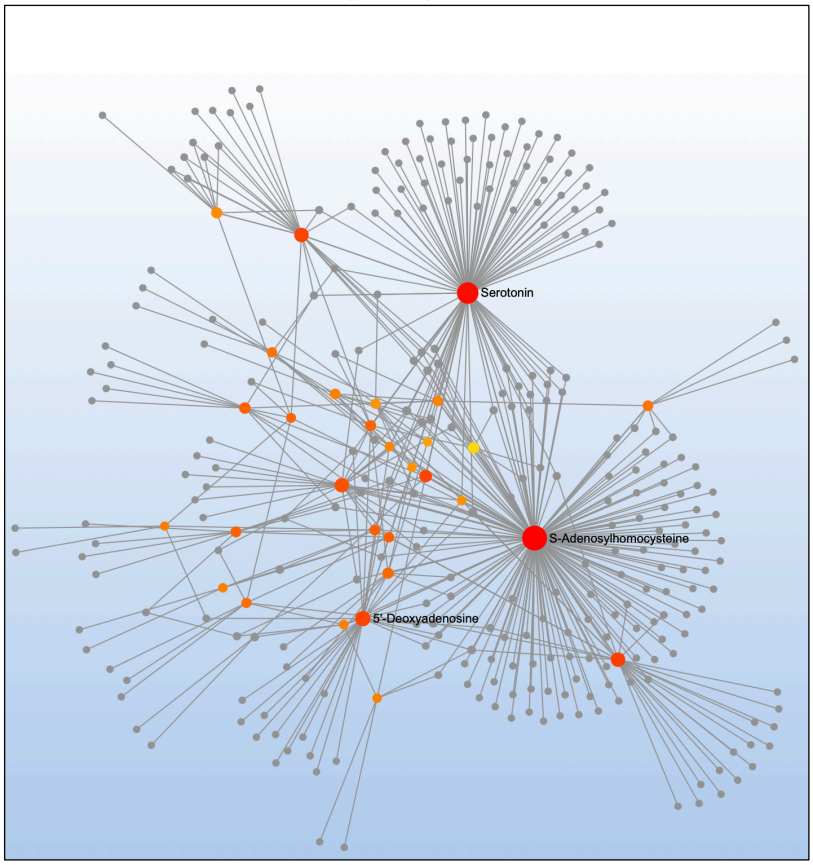

D

Metabolite-metabolite interaction network of metabolites identified in SOM for **day 5 to day 12**

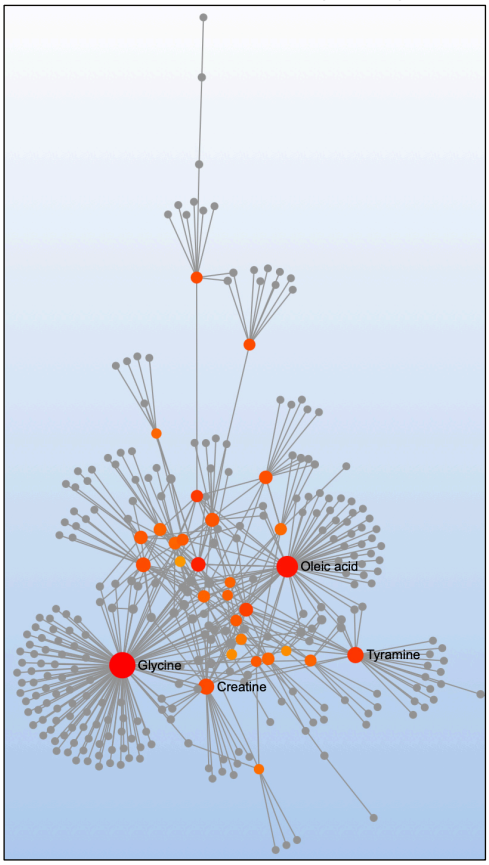

Figure S4. Related to Figure 4

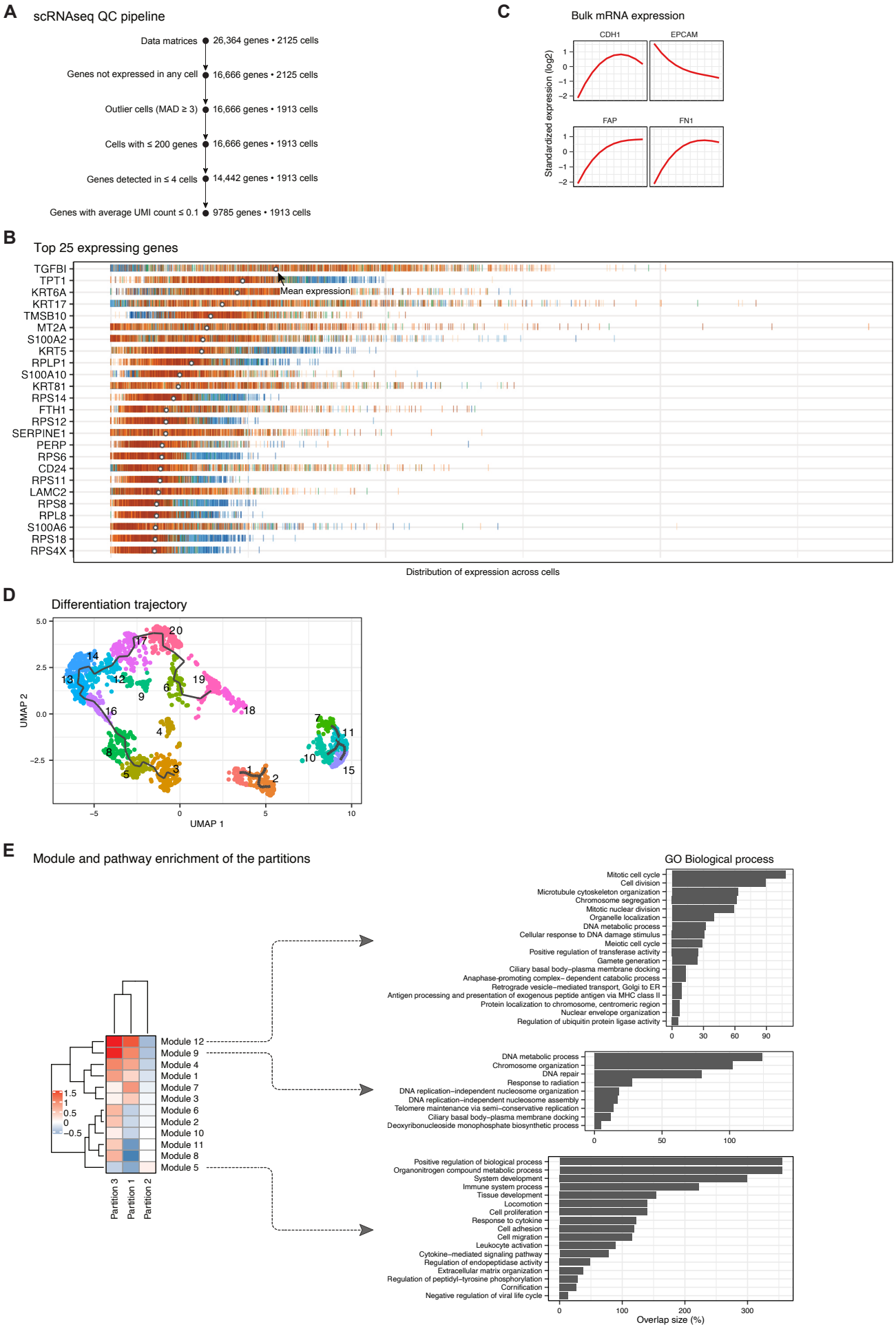

Figure S5. Related to Figure 5

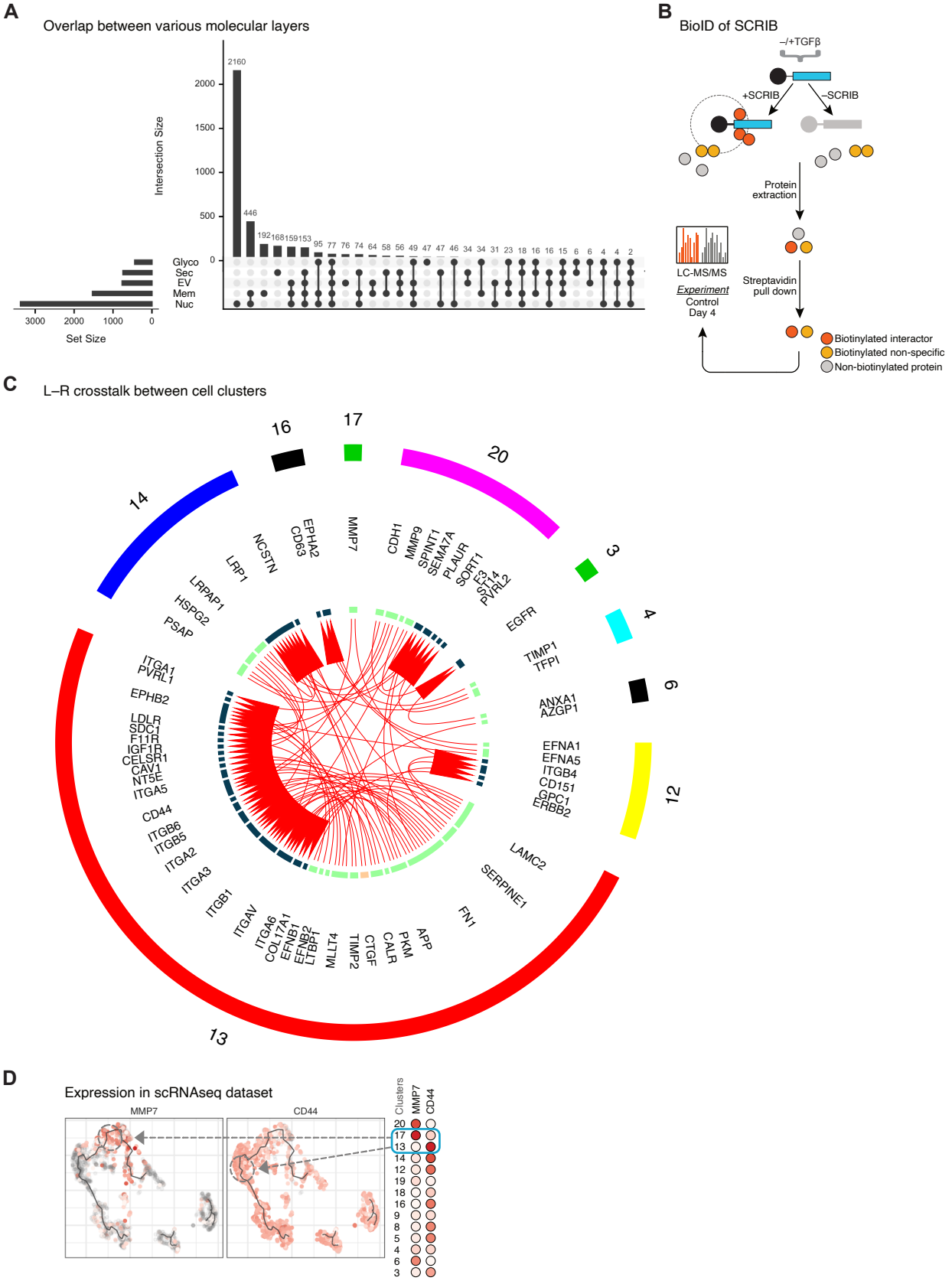
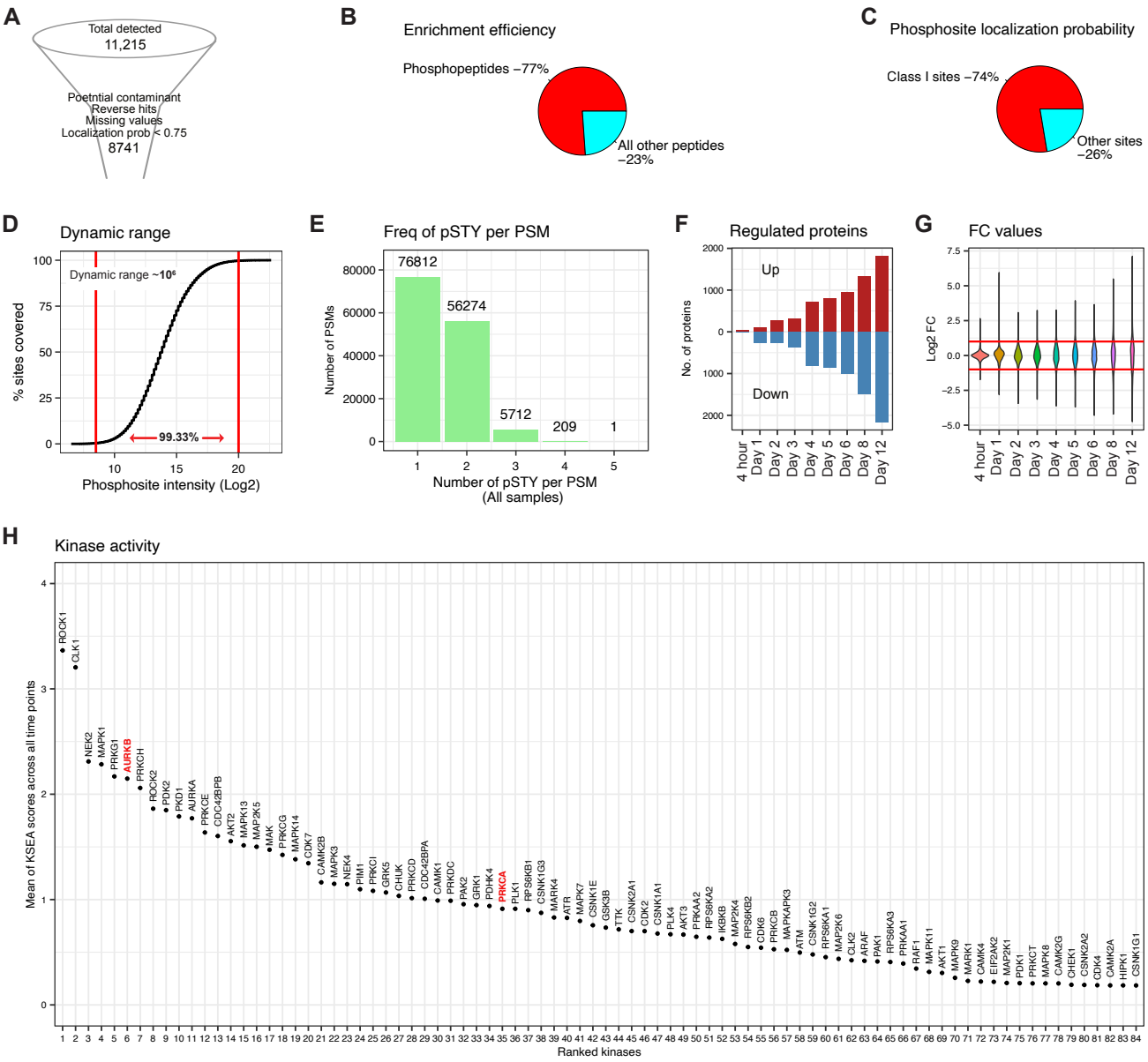
Figure S6. Related to Figure 6